



Evolution, Properties, and Spatial Variability of MJO Convection near and off the Equator during DYNAMO

WEIXIN XU AND STEVEN A. RUTLEDGE

Department of Atmospheric Science, Colorado State University, Fort Collins, Colorado

COURTNEY SCHUMACHER

Department of Atmospheric Sciences, Texas A&M University, College Station, Texas

MASAKI KATSUMATA

Japan Agency for Marine–Earth Science and Technology, Yokosuka, Japan

(Manuscript received 27 January 2015, in final form 11 July 2015)

ABSTRACT

This study investigates the evolution, structure, and spatial variability of Madden–Julian oscillation (MJO) convection observed during the 2011/12 Dynamics of the MJO (DYNAMO) field campaign. Generally, the C-band radars located in the near-equatorial Indian Ocean—Shared Mobile Atmospheric Research and Teaching Radar (SMART-R) on Addu Atoll (Gan) and NASA TOGA on the R/V *Roger Revelle* (*Revelle*)—observed similar trends in echo-top heights, stratiform rain fraction, and precipitation feature size across the MJO life cycle. These trends are closely related to changes in mid- to upper-tropospheric moisture, sea surface temperature (SST), zonal wind, and diagnosed vertical air motions. However, the evolution of convection, moisture, and vertical air motion at the R/V *Mirai* (*Mirai*), located in the intertropical convergence zone (ITCZ) at 8°S, exhibited a pattern nearly opposite to Gan and *Revelle*. When the MJO was active over the equator, convection was suppressed around *Mirai* owing to induced subsidence by the strong upward motion to the north. SST and zonal winds near *Mirai* were nearly invariant across the MJO life cycle, indicating little influence from the MJO in these fields. Compared to Gan and *Revelle*, *Mirai* had a significant amount of precipitation that fell from shallow and isolated convection. There were subtle differences in the evolution and properties of the convection observed between Gan and *Revelle*. Deep convection occurred slightly earlier at Gan compared to *Revelle*, consistent with the west-to-east progression of the MJO in the central Indian Ocean. Furthermore, convective deepening was more gradual over *Revelle* compared to Gan, especially during the October MJO event.

1. Introduction

The Madden–Julian oscillation (MJO) (Madden and Julian 1971, 1972) has broad impacts on the global weather and climate [see Zhang (2005, 2013) and references therein] such as monsoon rainfall variability, storm tracks, tropical cyclone frequency, tornado outbreaks, ENSO, intertropical convergence zone (ITCZ) convection, and extratropical climate modes. Despite decades of study, the MJO is still not well understood

and therefore MJO prediction skill is limited, especially concerning convective initiation over the equatorial Indian Ocean (IO) (Bechtold et al. 2008; Kim et al. 2009; Vitart and Molteni 2010). The 2011/12 Dynamics of the MJO (DYNAMO)/Cooperative Indian Ocean Experiment on Intraseasonal Variability in the Year 2011 (CINDY2011) field campaign (hereafter referred to as DYNAMO) was carried out to advance our understanding of the oceanic and atmospheric processes governing MJO initiation in the central IO (CIO) (Yoneyama et al. 2013). A complete set of observational facilities was deployed over the CIO during DYNAMO, including the central radar–sounding networks (based on islands, atolls, and ships), aircraft (dropsondes, airborne radar, and in situ), oceanographic instrumentation,

Corresponding author address: Weixin Xu, Department of Atmospheric Science, Colorado State University, 3915 West Laporte Avenue, Fort Collins, CO 80521.
E-mail: wxinxu@atmos.colostate.edu

and enhanced moorings (Yoneyama et al. 2013). More importantly, DYNAMO successfully observed three MJO events (Yoneyama et al. 2013; Gottschalck et al. 2013) during its intensive observing period (IOP; 1 October 2011–15 January 2012).

DYNAMO radar–sounding networks provide a rich dataset to investigate cloud population statistics, precipitation processes, and how these processes are related to MJO initiation and development (Johnson and Ciesielski 2013). Observations from multiwavelength radars at Gan Island and Addu Atoll [Gan; Fig. 3 in Yoneyama et al. (2013)] were employed to examine the full spectrum of MJO convective clouds. Measurements from the three radars (Ka, C, and S band) deployed on Gan were merged into a precipitating and nonprecipitating radar echo dataset (Feng et al. 2014). A convective and stratiform precipitation product based on the Ka-band cloud radar (KAZR) was also developed (Deng et al. 2014). These studies provided key information on the role of shallow and congestus clouds in the initiation of the MJO. Based on the S-band (S-Pol) radar measurements, Zuluaga and Houze (2013) found that rainfall in MJO active periods around Gan was intermittent and occurred in episodic bursts lasting 2–4 days. These convective events evolved in the order of shallow convective echoes (SCE), narrow and deep convective cores (DCC), wide convective cores (WCC), and broad stratiform regions (BSR). MJO-associated convective systems also exhibit different microphysical properties across their life cycle (Rowe and Houze 2014). In addition, the S-Pol analysis indicated that precipitation area, echo-top height, and tropospheric humidity rapidly increase over about 3–7 days prior to the MJO onset (Powell and Houze 2013). DePasquale et al. (2014) examined the cloud/precipitation and moisture evolution during the MJO events and convectively coupled Kelvin waves (KWs) using the Shared Mobile Atmospheric Research and Teaching Radar (SMART-R) also deployed on Gan. The KW moisture signatures were found to vary during different MJO periods (DePasquale et al. 2014). During the suppressed MJO period, moisture builds up vertically prior to the KW passage, but this signature was not clear during the developing and active MJO periods.

DYNAMO shipborne C-band radar measurements from the R/V *Roger Revelle* (*Revelle*) showed that convective deepening occurred during a period of 10–15 days prior to MJO onset (Xu and Rutledge 2014, hereafter XR14). This convective deepening period is consistent with atmospheric moistening time scales inferred from the DYNAMO sounding network (Johnson and Ciesielski 2013). XR14 composited the *Revelle* radar data as a function of MJO phase and identified strong correlations between convective populations and environmental

conditions, which were shown to be consistent with the so-called recharge–discharge process (Bladé and Hartmann 1993; Hu and Randall 1994; Kemball-Cook and Weare 2001). The precipitating cloud population consists of shallow isolated convective cells in suppressed phases, primarily isolated deep convective cells two phases prior to MJO onset, deep organized mesoscale convective systems (MCSs) in active MJO phases, and stratiform-dominant systems in decaying phases, followed by shallow, isolated convection. Guy and Jorgensen (2014) also found a similar shallow-to-deep-to-stratiform evolution of convective systems from analysis of airborne Doppler radar observations within the late November MJO event.

Convective organization and precipitation morphology have also been quantified using DYNAMO radar datasets. Zuluaga and Houze (2013) examined the frequency of convective systems during the MJO active periods with the organization of SCE, DCC, WCC, and BSR. Guy and Jorgensen (2014) investigated convective organization and dynamics using airborne radar data collected from the NOAA P-3 aircraft deployed in DYNAMO. They found that DYNAMO MCSs were organized more parallel to the low-level shear and produced weaker cold pools compared to MCSs observed in TOGA-COARE. Xu and Rutledge (2015, hereafter XR15) used the *Revelle* radar and Tropical Rainfall Measuring Mission (TRMM) Precipitation Radar (PR) datasets to investigate MJO-associated convective systems in specific organizational modes (MCS vs. sub-MCS, linear vs. nonlinear). Both the TRMM PR and the *Revelle* radar indicated that the occurrence and rainfall contribution of nonlinear MCSs were significantly higher compared to linear MCSs.

Yoneyama et al. (2013) provided an overview of MJO convection and environmental conditions from various DYNAMO observations. Johnson and Ciesielski (2013) showed the MJO properties and structures based on DYNAMO sounding networks. Both studies indicated significant temporal and spatial variations of convection during DYNAMO. However, the DYNAMO radar studies already reviewed were based on a single site and are not capable of addressing spatial variability. The current study is therefore intended to compare the properties of convection as simultaneously observed by the three DYNAMO C-band Doppler radars, situated at Gan, *Revelle*, and on board the R/V *Mirai* (*Mirai*). In this way, we can begin to investigate properties and spatial variations of the MJO convective behavior over a broader domain, even though the radar data are not continuous spatially. The ship-based radar–sounding observations along with those collected from Gan provide an extensive database on the vertical structure of precipitation—in particular, how shallow, congestus, and

deep clouds couple to changes in atmospheric humidity associated with MJO development over the CIO. The three C-band Doppler radars deployed in DYNAMO shared similar radar characteristics and scanning strategies by design. We will focus on the analysis of these C-band radars in a consistent manner to relate the spatial variability of precipitation, depth, and horizontal morphology of the precipitating clouds to atmospheric humidity, winds, and vertical motion patterns throughout the life cycle of the three MJO events observed during DYNAMO.

2. Data and methodology

This study is mainly based on satellite precipitation/cloud data and radar–sounding observations collected during DYNAMO. The TRMM 3B42 rainfall dataset and *Meteorological Satellite-7* (*Meteosat-7*) infrared (IR) measurements are used for the large-scale overview of precipitation and cloud evolution during DYNAMO. The three-dimensional structures of precipitating clouds and environmental conditions are examined using radar and sounding data collected from three of the DYNAMO research sites: Gan, *Revelle*, and *Mirai* (locations with circle in Fig. 2h). These research sites are located in the CIO approximately 800 km in distance from each other and cover different longitudes along the equator and locations near and off the equator.

a. Satellite products

1) TRMM 3B42 RAINFALL PRODUCT

The version 7 TRMM Multisatellite Precipitation Analysis (TMPA) 3B42 rain product (Huffman et al. 2007) is used to provide continuous rainfall time series and large-scale rainfall maps. The TMPA 3B42 data are available continuously from 1998 at 3-h temporal resolution and 0.25° spatial resolution. This dataset mainly uses TRMM PR observations and passive-microwave measurements from low-Earth-orbit satellites. The global tropics and subtropics are well covered (80%) by microwave data within a 3-h period. The infrared radiance measurements from geostationary satellites are used for rain estimation where there are no microwave data available. TMPA compares well with ground-based radar measurements over the tropical ocean (Huffman et al. 2007).

2) SATELLITE INFRARED DATA

We use IR (channel-8) measurements from *Meteosat-7* over the Indian Ocean (15°S–15°N, 50°–100°E) to examine the evolution of cold clouds during DYNAMO. Data were provided by the European Organization for the Exploitation of Meteorological Satellites (EUMETSAT). The IR data have a spatial resolution

of 5 km with a frequency of 30 min. The area of a cold cloud feature is defined as contiguous areas with a brightness temperature 208 K or colder, which is generally used for representing precipitating area (Chen et al. 1996; Kerns and Chen 2014).

b. DYNAMO sounding, SST, and lightning data

The DYNAMO sounding network (two quadrilateral arrays) included six research sites with four on islands and two on ships (Fig. 2h). This study uses sounding data collected from three sites where radar data are available: Gan (0.7°S, 73.1°E), *Revelle* (0°, 80.5°E), and *Mirai* (8°S, 80.5°E). Ship locations represent nominal positions when the ships were on station. For these sites, sounding data are available from four to eight times per day (see Table 1) with high vertical resolution (every 1–2 s) during the IOP (1 October 2011–15 January 2012) of DYNAMO (Ciesielski et al. 2014). Soundings and associated derived products have been rigorously quality controlled (Ciesielski et al. 2014). Vertical velocity was derived from sounding array data and supplemented with European Centre for Medium-Range Weather Forecasts (ECMWF) Operational Analysis when one or both research ships were offsite (<http://johnson.atmos.colostate.edu/dynamo/products/gridded/index.html>).

Two sea surface temperature (SST) datasets are employed in this study. One is the SST data collected from the Research Moored Array for African–Asian–Australian Monsoon Analysis and Prediction (RAMA) moorings (McPhaden et al. 2009) near *Revelle* and *Mirai*. Specifically, the 1-m-depth SST observed by RAMA is used. Satellite-based SST data are also used to provide the large-scale SST map during DYNAMO based on measurements from the TRMM Microwave Imager (TMI) and Advanced Microwave Scanning Radiometer for EOS (AMSR-E). These data are on a 0.25° × 0.25° grid and available daily (Gentemann et al. 2004, 2010).

Lightning strikes detected by Vaisala's GLD360 network are used for generating lightning frequency estimates. The GLD360 network detects cloud-to-ground (CG) and some intracloud (IC) strikes by measuring the magnetic field of radio impulses generated by lightning (Said et al. 2013). GLD360 has a global detection efficiency of about 60% for CG strikes and a location accuracy of about 2.5 km (Said et al. 2013). IC strikes are detected with a lower detection efficiency (~30%; Said et al. 2010).

c. DYNAMO radar data

During DYNAMO, C-band radars were deployed at Gan, as well as on board *Revelle* and *Mirai* (Fig. 2h). On Gan, SMART-R was operated by Texas A&M

TABLE 1. Summary of radar and sounding data used in this study (October–December 2011). Sample of radar precipitation feature (RPF) with an area larger than 20 km² is also included. Data are collected from Gan Island, R/V *Revelle*, and R/V *Mirai* during the intensive observing period of the 2011/12 DYNAMO field campaign. Normalized RPF sample is defined as total RPF number divided by radar operating time (day) and 360° radar area (radius of 150 km).

	Location			
	Gan Island		<i>Revelle</i>	<i>Mirai</i>
Sounding frequency	8 day ⁻¹		8 day ⁻¹ (4 day ⁻¹ during 17–31 Dec)	8 day ⁻¹
Radar	S-Pol (S band)	SMART-R (C band)	<i>Revelle</i> radar (C band)	<i>Mirai</i> radar (C band)
Radar operating time	1 Oct–31 Dec (92 days)	2 Oct–31 Dec (91 days)	2–29 Oct, 9 Nov–4 Dec, and 17–31 Dec (69 days)	1–25 Oct and 30 Oct–28 Nov (54 days)
Radar volumes	360° 4 h ⁻¹	180° 6 h ⁻¹	360° 6 h ⁻¹	360° 6 h ⁻¹
RPF samples (normalized)	124 853 (2035)	117 835 (2589)	236 229 (3423)	128 316 (2376)
Mean rain rate	—	6.9 mm day ⁻¹	7.8 mm day ⁻¹	4.5 mm day ⁻¹
Convective, stratiform rain fraction	—	69%, 31%	68%, 32%	75%, 25%

University. On board the R/V *Mirai*, the “*Mirai*” radar was operated by the Japan Agency for Marine–Earth Science and Technology (JAMSTEC). Finally, on the board the R/V *Revelle* the NASA TOGA radar (“*Revelle*” radar) was operated by Colorado State University and NASA. These three radars employed similar operational modes and scanning strategies. Analysis fields from the National Center of Atmospheric Research (NCAR) S band, polarimetric radar (S-Pol) on Gan are also used in this study. Operations of these C-band radars and S-Pol are summarized in Table 1. For consistency, similar quality control methods were applied to C-band radar data.

1) SMART-R AND S-POL ON GAN (0.6°S, 73.1°E)

Gan was referred to as a “radar supersite” during DYNAMO since three radars were deployed there, including the SMART-R, S-Pol, and KAZR (Ka-band vertically pointing radar; Feng et al. 2014). This study mainly compares the SMART-R with the other C-band radars. SMART-R is a C-band (5-cm wavelength) mobile Doppler radar (Biggerstaff et al. 2005), which operated on the northwest end of Addu Atoll (Feng et al. 2014; DePasquale et al. 2014) from 1 October 2011 through 9 February 2012. During DYNAMO, SMART-R ran on a 10-min scan cycle that included a merged volume scan with 25 elevation angles (0.5°–33°) to a range of 150 km, followed by three vertical cross section scans selected by radar scientists (RHIs; Feng et al. 2014). SMART-R calibration and quality control was conducted by Texas A&M (Fliegel 2012). The data used in this study take into account a 1.5° tilt offset that was discovered after the creation of first quality controlled dataset (DePasquale et al. 2014). Because of beam blockage, radar data have only been analyzed in a 180°

sector defined by the azimuth interval from 338° and 158°.

The NCAR S-Pol radar was deployed approximately 3 km south of SMART-R from 1 October 2011 through 15 January 2012. S-Pol is an S-band (10-cm wavelength), polarimetric, Doppler radar having an 8.5-m antenna with a 0.91° beamwidth. During DYNAMO, S-Pol operated on a 15-min scanning cycle including a 360° plan position indicator (PPI) volume scan consisting of eight elevation angles (0.5°–11°) followed by a large number of RHIs (Yoneyama et al. 2013; Feng et al. 2014), all out to 150 km. The S-Pol calibration and data quality control was conducted by NCAR (Feng et al. 2014).

2) C-BAND RADAR ON BOARD REVELLE (0°, 80.5°E)

The *Revelle* (Moum et al. 2014) was deployed at the east-central site of the DYNAMO sounding array over the CIO (Yoneyama et al. 2013). During DYNAMO, *Revelle* made four cruises to the campaign area (XR2014) from September 2011 to January 2012. This study only analyzes measurements obtained during cruises 2–4 (October–December 2011). Data are not included when the ship was transiting to or from port or otherwise off station (Table 1). The *Revelle* radar operated round the clock when the ship was on station (XR14). The *Revelle* radar completed a full scan cycle every 10 min including a 360° PPI volume with 22 sweeps (0.5°–42°) and 5 RHIs (XR14), each out to 150 km. The *Revelle* radar data were calibrated and quality controlled by the Radar Meteorology Group at Colorado State University and NASA (see XR14 for details). A C-band attenuation correction algorithm was derived from drop size distribution (DSD) measurements on

Gan during DYNAMO and a longer term record at Manus Island in the western Pacific (Thompson et al. 2015) and is considered to be an improvement over past methods. The previously used method estimates rain rate R from uncorrected reflectivity then estimates attenuation A from the rain rate in order to correct the original reflectivity (Z) field. Errors and uncertainties can arise in estimating rain rate from uncorrected Z and dealing with uncertain Z – R and A – R relationships. However, the method (A – Z) used in this study directly corrects Z from an attenuation factor calculated from drop size distribution data obtained in DYNAMO. Scattering theory was used to relate path attenuation directly to water contents derived from the DYNAMO DSD data.

3) C-BAND RADAR ON BOARD *MIRAI* (8°S, 80.5°E)

The *Mirai* was deployed at the southeast site of the DYNAMO sounding array. During DYNAMO, the *Mirai* made two cruises to the campaign area from late September to early December 2011 (Yoneyama et al. 2013). To conduct comparisons with observations over Gan and *Revelle*, this study only includes *Mirai* radar measurements taken from October through December 2011. Like the *Revelle*, radar data were excluded when the ship was transiting to or from port or otherwise off station (Table 1). The C-band radar on board the *Mirai* (hereafter called the *Mirai* radar) operated round the clock when the ship was on station. The *Mirai* radar completed a full scan cycle every 10 min including a 360° PPI volume with scans of 21 elevations (0.5°–40°) and several RHIs in the range of 160 km. *Mirai* radar data were calibrated and quality controlled by JAMSTEC [details in Katsumata et al. (2008)]. *Mirai* has followed similar data quality controls as *Revelle*—for example, both using the same attenuation correction algorithm.

4) RADAR-DERIVED PRODUCTS

After quality control, the same gridding method, convective–stratiform classification, rainfall estimation relationships, and echo-top method were applied to all three C-band radars as well as S-Pol. Radar polar coordinate data were interpolated to Cartesian coordinates using the NCAR REORDER software package (Oye and Case 1995), with a resolution of 2 km in the horizontal and 0.5 km in the vertical. Radar reflectivity was then classified into convective and stratiform precipitation components based on Steiner et al. (1995). The Z – R relationships are $Z = 134R^{1.44}$ and $Z = 300R^{1.55}$ for convective and stratiform rain, respectively. As with the attenuation coefficients, these Z – R relationships were derived from DSD measurements from Gan and Manus Island (Thompson et al. 2015). Echo-top heights of specific echo intensities

(e.g., 0 dBZ) are obtained by finding the maximum height of that value in the particular grid column. Analysis of the precipitation map and echo-top heights was limited to 120 km from each radar considering the coarse resolution (horizontal of 3 km and vertical of 1.5 km) of the raw data outside this range. The calculation of echo-top heights was further constrained to 20–120-km range because of storm-topping issues close to the radar.

This study also delineates radar precipitation features (RPFs) to analyze precipitation morphology. For this purpose, the echo object identification method used in the TRMM PF database (Nesbitt et al. 2006; Liu et al. 2008) was applied. Specifically, RPFs are defined as contiguous radar pixels exceeding the 20-dBZ threshold at a 2-km altitude (XR15). XR15 showed that the *Revelle* radar and TRMM PR observed similar PF patterns. The size of an RPF is defined as its total area of pixels great than 20 dBZ. Since radar resolution is less important for calculation of RPFs, the RPF algorithm was applied to the full radar range (150 km). The number of RPFs sampled by each radar is listed in Table 1.

d. MJO indices

This study also conducts MJO composites of multiple parameters. MJO phase is defined by the Wheeler–Hendon Real-Time Multivariate MJO index (Wheeler and Hendon 2004, hereafter WH index). The WH index is based on the combined empirical orthogonal functions (EOFs) of large-scale outgoing longwave radiation (OLR) and zonal wind fields at 850 and 200 hPa. The WH index has been widely used and is an effective filter for intraseasonal frequencies associated with the MJO (Lau and Wu 2010; Riley et al. 2011). According to the WH index, each day in the tropics can be assigned to one of eight MJO phases. Parameters including 20-dBZ echo-top heights, areal-mean rainfall, stratiform rain fraction, lightning frequency, and SST are averaged during multiple days in a specific MJO phase. There are a large number of data samples in each MJO phase, especially for Gan (Powell and Houze 2013) and *Revelle* (XR14). The sample distribution is relatively uneven though; for example, most data of MJO 3 (mid-December–early January 2011) are distributed in phases 4 and 5 (XR14).

3. Large-scale satellite overview

DYNAMO IOPs observed three intraseasonal and eastward-propagating large-scale convective events (namely MJOs). The first two MJO events in October (MJO 1) and November (MJO 2) were prominent and coherent with wind signals circumnavigating the globe, whereas the December MJO (MJO 3) was less coherent with an incomplete global cycle. The large-scale conditions

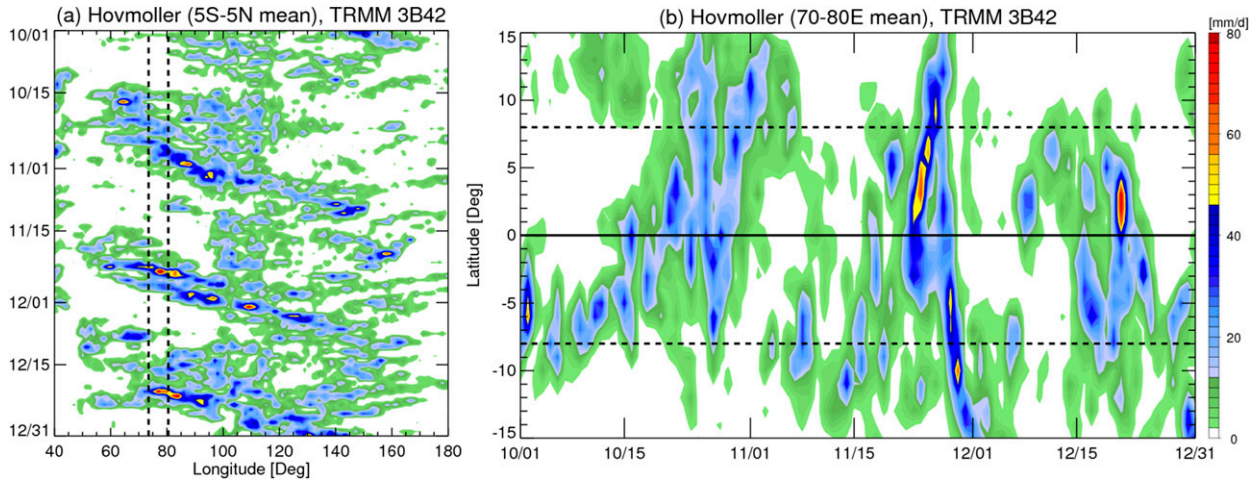


FIG. 1. Hovmöller diagram of TRMM 3B42 rainfall (mm day^{-1}) during October–December 2011 (a) as a function of longitude (5°S – 5°N average) and time with dashed lines indicating west and east boundaries of DYNAMO array, and (b) as a function of latitude (70° – 80°E average) and time with dashed lines representing southern and northern boundaries of DYNAMO array.

of the atmosphere and upper ocean during these MJO events were examined in detail by Gottschalck et al. (2013) and Johnson and Ciesielski (2013). This section provides a general overview of the evolution and spatial variations of rainfall, cold cloud patterns, and SST during the three MJO events.

a. Rainfall

Figure 1 provides the time–longitude and time–latitude depiction of precipitation over the tropical IO from October to December. Both time–longitude and time–latitude cross sections show three enhanced precipitation periods associated with the three MJOs. The intervals of these MJO events are about 30 days. The time–longitude cross section (Fig. 1a) clearly shows that MJO heavy precipitation initiated over the western IO, passed through the DYNAMO arrays (dashed lines), and propagated eastward to the Maritime Continent. However, these MJO heavy precipitation events faded over the western Pacific, probably as a result of La Niña conditions over the Pacific at that time (Gottschalck et al. 2013). Prior to the MJO 1 rainfall peak, the precipitation pattern showed a pronounced northward shift from the usual latitude of the ITCZ in the Indian Ocean between 5° and 10°S (Waliser and Gautier 1993) toward the equator (Fig. 1b). This pattern was less evident before MJO 2 and 3. Kerns and Chen (2014) suggested that dry-air intrusion from the subtropics into the equatorial region played a key role in the convective initiation and evolution of MJO 2. This dry-air intrusion suppressed convection in the ITCZ. Therefore, subsidence on the equator due to ITCZ convection to the south was reduced (see Fig. 12), leading to an equatorward shift of convection.

Figure 2 displays a panel view of the composite MJO precipitation as a function of MJO phase. A well-defined heavy precipitation envelope on the scale of approximately 1000 km developed in phase 1 over the western IO with the edge reaching the western boundary of DYNAMO (Fig. 2a). Prior to the onset of MJO convection (e.g., phases 6–8), enhanced precipitation was only present south of the equator (south of 5°S) associated with ITCZ convection, while convection in the IO region near and north of the equator was highly suppressed (Figs. 2f–h). During this period, the southern portion of the DYNAMO sounding network, including the *Mirai* location, was experiencing ITCZ convection (Figs. 2f–h). Heavy precipitation associated with the MJO propagated into the DYNAMO region in phase 2. The heaviest precipitation was north of the equator but nonetheless significant precipitation occurred at Gan and the *Revelle* (Fig. 2b). In contrast, convection around the *Mirai* was notably absent during MJO phases 1 and 2 (Figs. 2a,b).

The heaviest precipitation propagated to the eastern IO in phase 3 (Fig. 2c). The eastern IO actually received the most rainfall in the basin. This heavy precipitation may have been caused by eastward-moving MJO precipitation interacting with the westward migration of convection from Sumatra (Mori et al. 2004; Sakurai et al. 2005; Fujita et al. 2011). Diurnal convection generated over Sumatra propagates westward with easterly steering level winds. However, precipitation, although not as heavy as phase 2, remained over the DYNAMO region during phases 3 and 4 (Figs. 2c,d), which was contributed substantially by stratiform precipitation (XR14). Phase 4 rain rates might be somewhat biased, considering the active period of MJO 3 was defined as phase 4 by WH

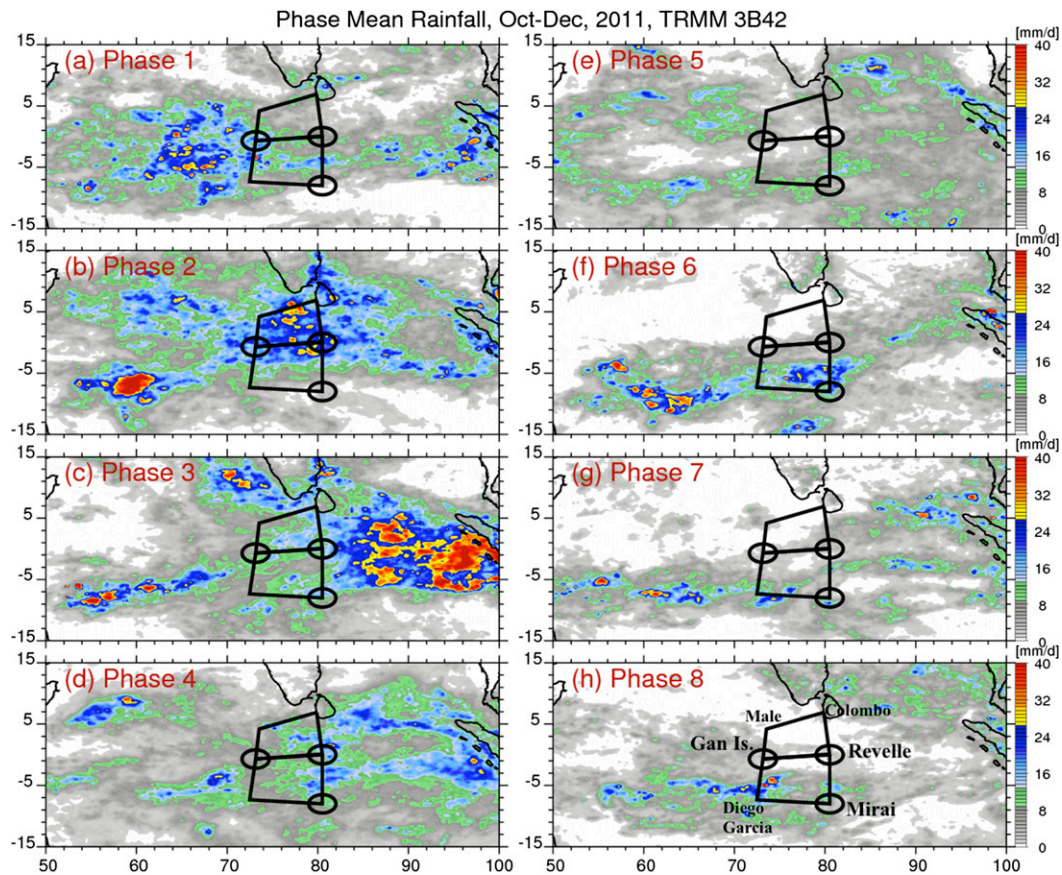


FIG. 2. TRMM 3B42 rainfall (mm day^{-1}) composited by WH MJO phase during October–December 2011. Black boxes indicate DYNAMO sounding arrays, and black circles define approximate radar ranges. Names of specific radar-sounding sites are marked in (h).

index (XR14). Spatial variability of rainfall is evident throughout the MJO life cycle—for example, Gan and *Revelle* at the equator versus *Mirai* at the ITCZ or Gan at the western side versus *Revelle* and *Mirai* at the eastern side of the DYNAMO domain. It is also worth noting that ITCZ convection was evident during all MJO phases over the western IO south of the equator.

Precipitation variations at Gan, *Revelle*, and *Mirai* are also shown in the rainfall time series averaged over a $500 \text{ km} \times 500 \text{ km}$ box around these sites (based on TRMM 3B42; Fig. 3). (Note that the TRMM rainfall averages used the nominal positions of the ships.) Rainfall along the equator (Gan and *Revelle*) showed a different trend from that at *Mirai* during MJO 1 (October) and MJO 2 (November), but all sites shared a similar rainfall trend during MJO 3 (December). Although Gan experienced a generally similar precipitation time series to that at *Revelle*, precipitation maxima over Gan appeared to oscillate more frequently than over *Revelle* (e.g., from 15 October to 1 November). During MJO 1, Gan experienced six to seven pulses of

heavy rainfall lasting 2–4 days (Zuluaga and Houze 2013), whereas *Revelle* observed only three to four episodes of heavy rainfall. Certain rainfall breaks during active periods of MJO 2 were postulated to be caused by dry-air intrusions (Kerns and Chen 2014). During MJO 2, both Gan and *Revelle* observed two substantial rainfall peaks (after 20 November) owing to the passage of Kelvin waves (Johnson and Ciesielski 2013; Gottschalck et al. 2013; DePasquale et al. 2014). The second Kelvin wave in MJO 2 also produced a rainfall peak over the nominal *Mirai* location (8°S , 80.5°E). Note that *Mirai* was no longer on site when the second Kelvin wave arrived. On the other hand, MJO 3 generated two major periods of rainfall over all three sites. As shown in Fig. 1b, the onset of the heavy precipitation of MJO 3 was sudden, covering both the equator and the ITCZ.

b. Cold cloud features

The evolution (as a function of MJO phase) of cold cloud features (Fig. 4) matches well with the rainfall

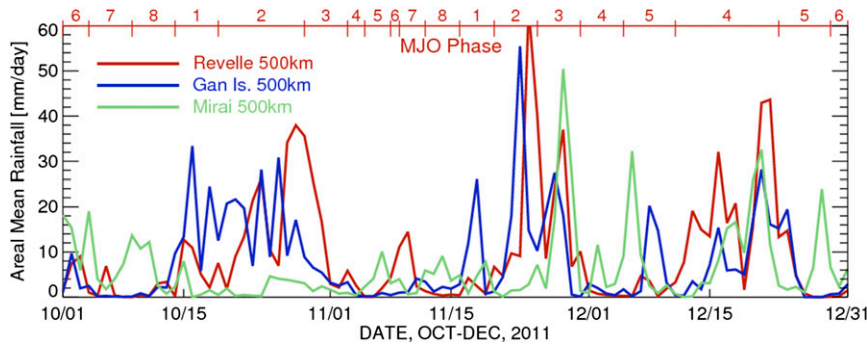


FIG. 3. Time series of daily mean rainfall based on TRMM 3B42 in $500 \text{ km} \times 500 \text{ km}$ boxes centered at Gan Island (blue), R/V *Revelle* (red), and R/V *Mirai* (green). The upper x axis indicates the WH MJO phase. Note that rainfall averages for the ships (*Revelle* and *Mirai*) were computed for their nominal positions.

evolution (Fig. 2). During the suppressed phases (phases 6–8; Figs. 4f–h), cold cloud tops were rare around the equator, and if any were present, they were isolated. During these phases, the ITCZ region between 5° and 10°S (Waliser and Gautier 1993) was always covered by an enhanced amount of cold cloud, though isolated. Both the population and horizontal extent of cold cloud features increased dramatically in phase 1 (Fig. 4a), mainly to the west of the DYNAMO array where the MJO heavy precipitation initiates (Figs. 1a and 2a). As the MJO convective envelope propagated eastward (phase 2; Fig. 4b), cold cloud features became more numerous and larger in extent (e.g., reaching the size of large MCSs; $>20000 \text{ km}^2$ as shown by red circles in Fig. 4). Cold clouds concentrated over the central and northern portions of the DYNAMO region, with more large MCS-like cloud features passing over *Revelle* compared to Gan. No large cold cloud features were observed near the *Mirai* during phase 2 (e.g., all features larger than 20000 km^2 were located to the north). Cold clouds remained broad in size (Fig. 4c) even when the MJO precipitation reduced substantially over the DYNAMO arrays in phase 3 (Fig. 2c), mainly as a result of the more stratiform nature of the precipitation during this phase (XR14). Cold clouds were still frequent during the decaying phase over the CIO (phase 4; Fig. 4d), but coverage was sparse. The equatorial IO returned to suppressed conditions in phase 5 with a notable absence of cold cloud features (Fig. 4e).

c. Sea surface temperature

Figure 5 shows the large-scale satellite-observed SST patterns over the IO. An SST ridge is evident around the equatorial IO. SST variability (as a function of MJO phase) within the ridge is greater than outside the ridge. This SST ridge is consistent with the presence of the Seychelles–Chagos thermocline ridge (Vialard

et al. 2008) in the central IO. Increases in SST over the equatorial IO preceded the rainfall maxima there (Fig. 2) by one to two phases. For example, SSTs over the DYNAMO region began increasing starting from the most suppressed phase (phase 6; Fig. 5f), peaking one phase prior to the active MJO period (phase 1; Fig. 5a). Similar to the precipitation trend, SSTs over the western IO peaked one phase earlier than in the eastern CIO. SSTs decreased soon after the onset of the MJO (phase 2) and reached minimum values during phases 4 and 5. This SST evolution is consistent with SST measurements made at the *Revelle* (Moum et al. 2014; XR14). Several factors were attributed to the sharp reduction in SST due to the MJO: reduction in solar insolation from increased cloudiness, widespread rainfall, the entrainment of cooler subsurface water to the ocean surface owing to shear driven mixing, and enhanced heat fluxes out of the ocean (Moum et al. 2014). On the regional scale, Gan and *Revelle* experienced higher SSTs (especially during phases 8, 1, and 2) and experienced greater SST variability due to MJO passage compared to the trends at the *Mirai*.

4. Observations from DYNAMO radar–sounding arrays

This section presents precipitation and convective properties of precipitating clouds as well as environmental conditions based on radar and sounding data collected from the three radar sites.

a. Radar-estimated rainfall

On average, there was much more rainfall over the equatorial radar sites at SMART-R (6.9 mm day^{-1}) and *Revelle* (7.8 mm day^{-1}) compared to the off-equatorial site *Mirai* (4.5 mm day^{-1}) (Table 1). The mean stratiform rain fraction was also 6%–7% larger for the

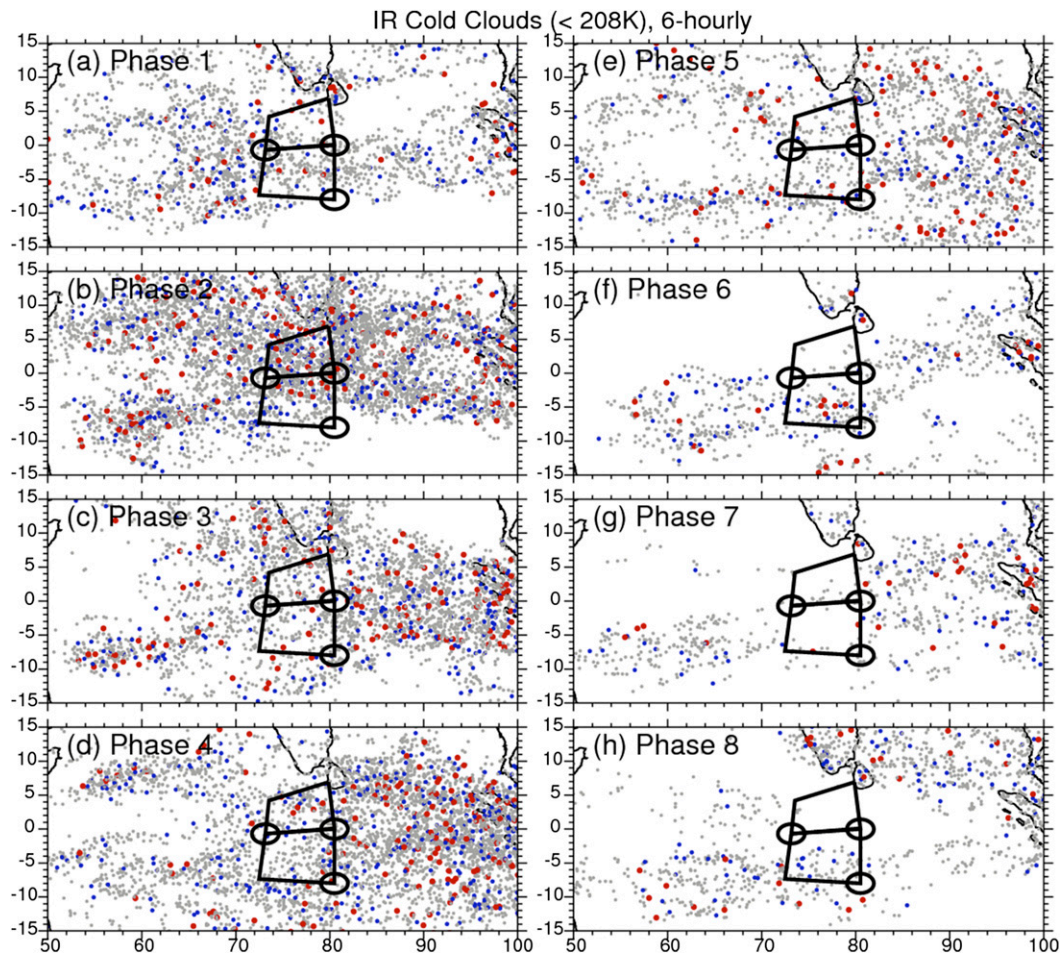


FIG. 4. Distribution of cold cloud features (clusters with boundaries of 208-K IR brightness temperature) every 6 h as a function of WH MJO phase (phases 1–8) during October–December 2011. The size of filled circles is indicated by colors: gray ($< 5000 \text{ km}^2$), blue ($5000\text{--}20\,000 \text{ km}^2$), and red ($> 20\,000 \text{ km}^2$).

equatorial sites compared to the *Mirai* location (Table 1). Figure 6 shows rainfall time series estimated by SMART-R and the *Revelle* and *Marai* radars, which are qualitatively similar, at least in terms of the overall pattern and variability, to the TRMM 3B42 time series (Fig. 3). Precipitation maxima derived from the *Revelle* radar and SMART-R (Fig. 6) were smaller than those determined by TRMM 3B42 (Fig. 3), mainly because the heaviest precipitation fell north of the equator, beyond the ranges of these radars (Fig. 2). SMART-R and *Revelle* observed three major periods of heavy precipitation associated with the three MJO events (Figs. 6a,b), while the *Mirai* radar documented a very different pattern (Fig. 6c), especially for MJO 1. For the MJO 1 period, *Mirai* rain led the rain patterns at Gan and *Revelle*, consistent with the northward and eastward shift of the ITCZ convection to the equator. Such a shift was less evident for MJO 2 (Fig. 1b), where rain peaks in the *Mirai* record occurred nearer in time to those at Gan and *Revelle*. The fraction of

stratiform rain (red dashed lines) over SMART-R and *Revelle* increased substantially with the onset of each MJO; for example, only 20% of the total rain was due to stratiform precipitation in suppressed periods compared with 45%–50% in active periods. Large stratiform precipitation fractions are typical in active MJO periods (Lin et al. 2004; XR14), because precipitation systems during these periods are well organized (XR15) as the environmental conditions [moderate convective available potential energy (CAPE), moist troposphere, and significant deep shear] are favorable for stratiform precipitation development (Halverson et al. 1999; Saxen and Rutledge 2000). In contrast, the stratiform fractions at *Mirai* were consistently lower ($\sim 20\%$) during most of the time series, with the exception of the two heavy precipitation periods in early October ($\sim 35\%\text{--}40\%$).

Differences in the rainfall patterns were also observed between SMART-R (west) and *Revelle* (east), both along the equator. For MJO 1, precipitation in range of

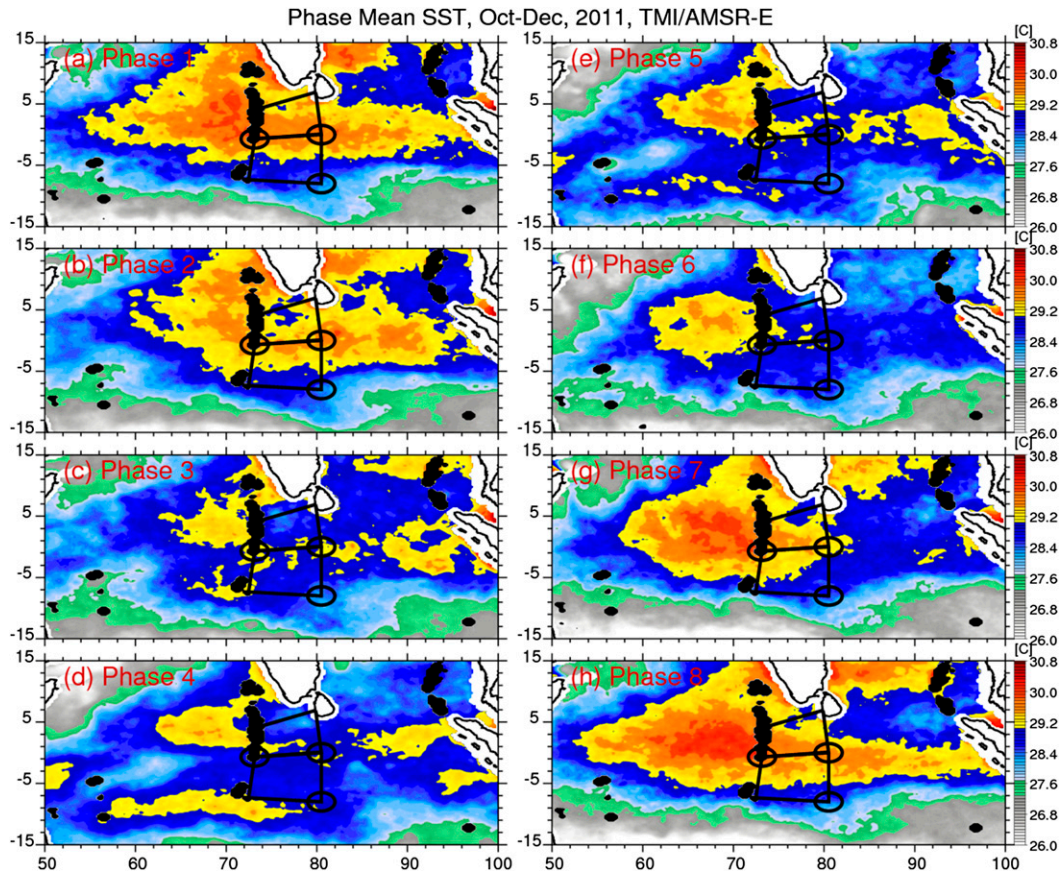


FIG. 5. Satellite-estimated daily mean SST ($^{\circ}\text{C}$; TMI/AMSR-E) composited by WH MJO phase (phases 1–8) during October–December 2011.

the SMART-R (i.e., MJO 1) maximized at phase 1 associated with the MJO onset over the western tropical IO (Fig. 2a). Precipitation over *Revelle* peaked one phase later (phase 2) after the core MJO convection propagated to the east (Fig. 2b). However, for MJO 2, *Revelle* and SMART-R both experienced peak rainfall during phase 2. For MJO 1, rainfall peaked early at SMART-R then decreased gradually. At *Revelle*, rainfall continuously increased associated with a building MJO. For MJO 2, both radars observed similar patterns dominated by the double peaks in rainfall associated with the passage of the two Kelvin waves in late November. The increase in rainfall from minimum to maximum values was more gradual and persistent in the *Revelle* radar time series (~ 2 weeks) compared to SMART-R (~ 10 days). S-Pol observations over Gan showed that precipitation area, radar echo-top height, and tropospheric humidity rapidly increased over about 3–7 days prior to the MJO onset (Powell and Houze 2013). SMART-R observed a higher frequency of rainfall maxima compared to *Revelle*, particularly during MJO 1 (also seen in Fig. 3). Precipitation over SMART-R showed a 2-day oscillation while the

Revelle site experienced 3–5-day rainfall maxima. These rainfall oscillations were possibly associated with the passage of equatorial Rossby waves (Gottschalck et al. 2013; Zuluaga and Houze 2013). However, it is unclear why the rainfall oscillations between Gan and *Revelle* were indeed different. Though MJO 3 produced similar rainfall amounts as MJO 1 and 2 on the larger scale (Fig. 3), SMART-R and *Revelle* observed much less rainfall during MJO 3 compared to MJOs 1 and 2 (Figs. 6a,b). It should be noted that SMART-R and *Revelle* may not be generally representative of MJO precipitation during MJO 3, since MJO 3 did not significantly impact Gan or *Revelle*, with the heavy precipitation passing to the north of these locations. *Mirai* was not on station during MJO 3. In fact, large-scale satellite rainfall estimation indicated that MJO 3 produced rainfall peaks with similar magnitude as MJO 1 and 2.

b. Radar echo-top heights and precipitation morphology

Figure 7 depicts time series of radar echo-top (0 dBZ) heights indicating the evolution of the depth

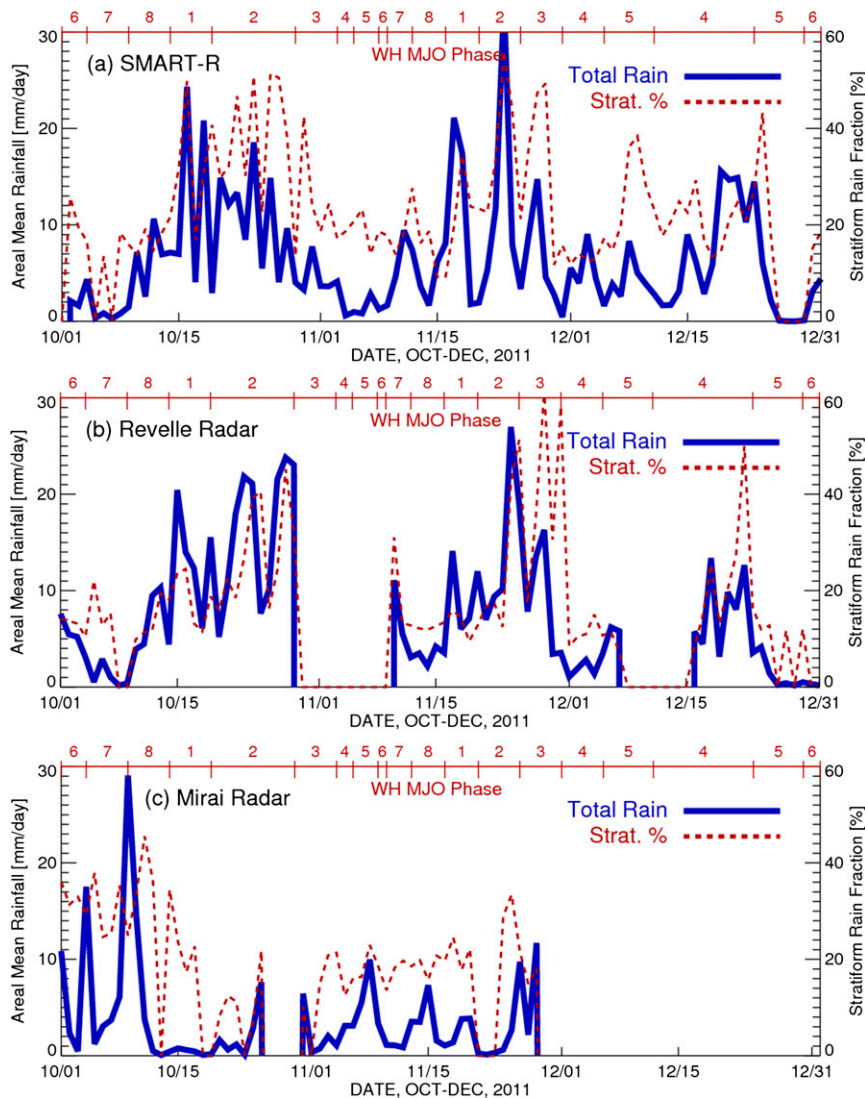


FIG. 6. Time series of total rainfall and stratiform rain fractions derived from radars: (a) SMART-R (Gan), (b) *Reville*, and (c) *Mirai*. The upper x axis (red) indicates the WH MJO phase. Note that there are data gaps for *Reville* (30 Oct–8 Nov and 5–16 Dec 2011) and *Mirai* (26–29 Oct and after 29 Nov 2011).

of precipitating clouds. Echo-top height evolution shows clear deepening and decaying of convective clouds across the MJO life cycle over SMART-R (Fig. 7a) and *Reville* (Fig. 7b) locations (see Fig. 1), but with a dominance of shallow convection with sporadic deep convection over *Mirai* (Fig. 7c). Echo-top heights correlate fairly well with the precipitation totals ($R = 0.73$ – 0.79 at 95% confidence) at all locations; for example, echo tops peaked (decreased) when precipitation maximized (minimized; Fig. 6). During suppressed MJO periods, the mean echo-top heights over SMART-R and *Reville* were mostly below the freezing level (5 km). However, *Mirai* radar observations were dominated by shallow clouds with mean echo-top heights of 3–4 km.

Convective deepening over the *Reville* radar was somewhat more gradual (e.g., ~ 2 weeks for MJO 1) than over SMART-R (~ 10 days for MJO 1). The convective deepening period for MJO 2 was somewhat more abrupt at both SMART-R and *Reville* locations (~ 5 – 7 days).

Figure 8 shows the variations in precipitation feature size (RPFs) at all three locations. Note that RPFs based on S-Pol instead of SMART-R are used here, since the SMART-R scan sector was limited to 180° (described in section 2b). Deep convection (e.g., during active MJO periods; Fig. 7) was well correlated with precipitation systems of large horizontal extent (Fig. 8). This plot also clearly shows the isolated nature of precipitating clouds during suppressed MJO periods over Gan (S-Pol) and

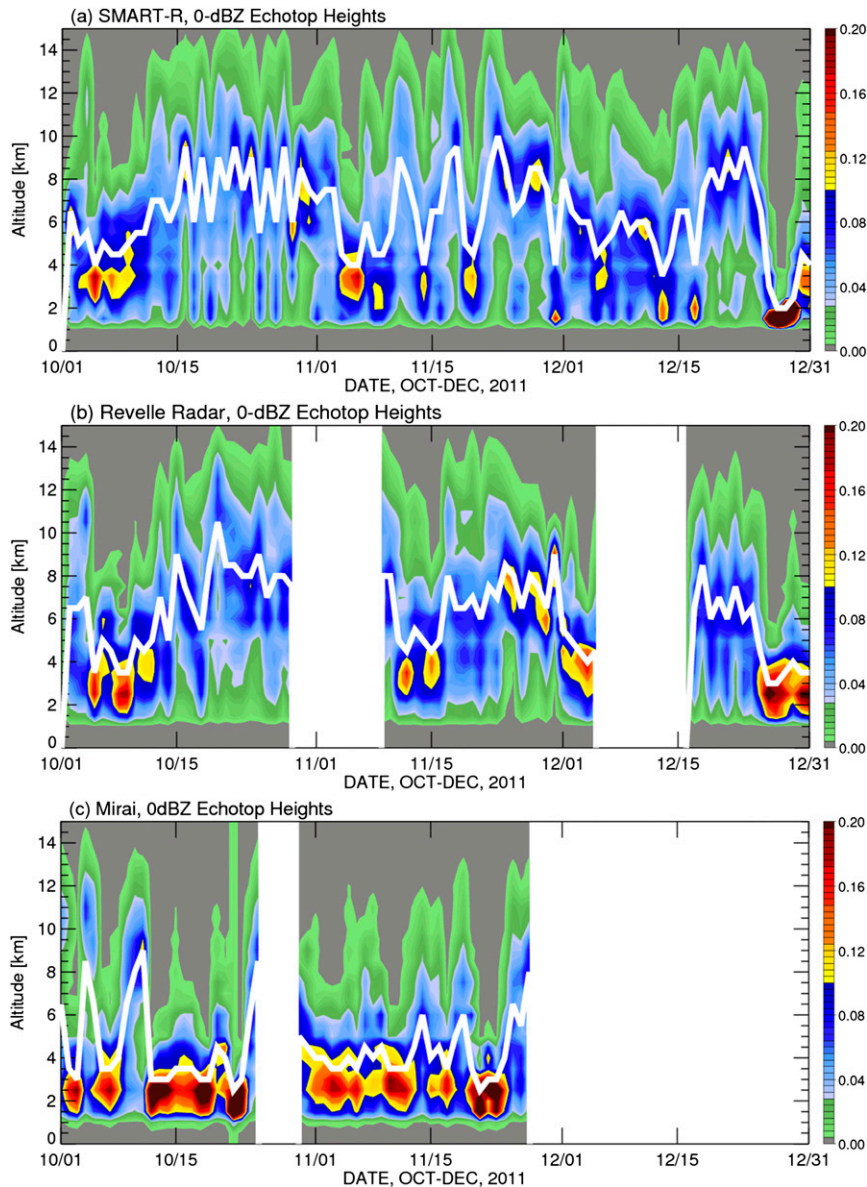


FIG. 7. Time series of radar 0-dBZ echo-top heights derived from radars: (a) SMART-R (Gan), (b) *Reville*, and (c) *Mirai*. Color shade indicates the occurrence frequency, and the white solid curve represents the mean value. Note that there are data gaps for *Reville* (30 Oct–8 Nov and 5–16 Dec 2011) and *Mirai* (26–29 Oct and after 29 Nov 2011).

Reville, and nearly all of the time at *Mirai*. These isolated precipitating clouds were narrow, being less than 10 km in width, in contrast to broad systems (~ 100 km in width) during active periods of MJO precipitation.

The contrast between Gan/*Reville* and *Mirai* is evident in terms of precipitation frequency as a function of convective depth and precipitation morphology (Fig. 9). Shallow and isolated convection dominated the *Mirai* observations compared to relatively deep and organized systems over Gan and *Reville*. Approximately 40% of the radar echoes at *Mirai* were shallow,

warm-rain cells (i.e., echo top < 5 km), compared to just 20% at Gan and *Reville* (Fig. 9a). In addition, 50% of the feature sizes near *Mirai* were smaller than 1000 km^2 , compared to only 30% at Gan (represented by S-Pol) and *Reville* (Fig. 9b). Note that feature sizes derived from SMART-R were relatively smaller than S-Pol (both in Gan) as SMART-R data were restricted to the eastern 180° radar sector considering radar beam blockage at the west. On the other hand, large MCSs (i.e., width > 100 km) contributed more than 40% of the precipitation frequency over Gan

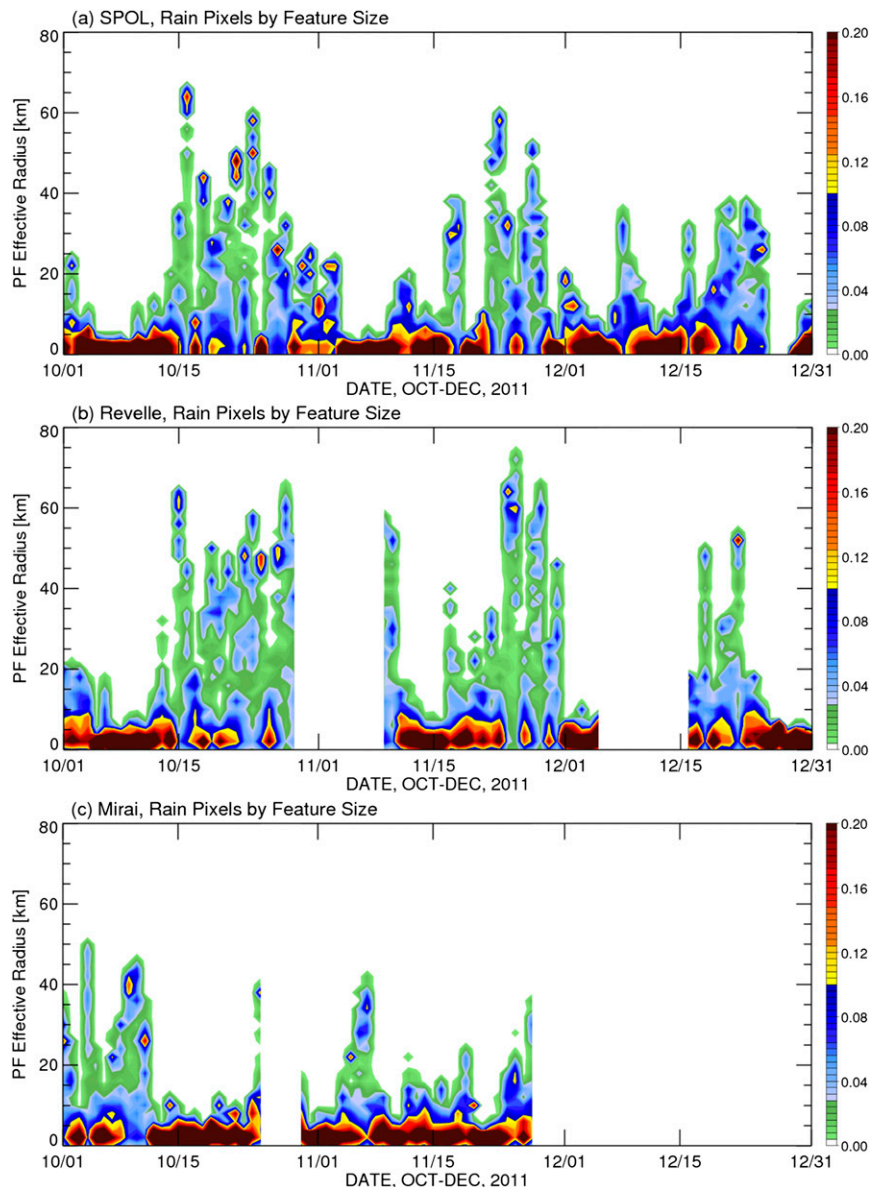


FIG. 8. Time series of precipitation frequency as a function of precipitation feature size (effective radius of the feature area) based on radars: (a) S-Pol (Gan), (b) *Reville*, and (c) *Mirai*. Note that there are data gaps for *Reville* (30 Oct–8 Nov and 5–16 Dec 2011) and *Mirai* (26–29 Oct and after 29 Nov 2011).

and *Reville*, whereas they produced only 20% of precipitation frequency over *Mirai*.

c. Environmental conditions

The tropospheric moisture patterns (Fig. 10) closely resemble those of echo-top heights (Fig. 8). The lowest levels (1000–900 hPa) of the troposphere were relatively moist across the entire period owing to evaporation from the warm sea surface. The mid- to upper troposphere over Gan and *Reville* (Figs. 10a,b) was extremely dry during convectively suppressed periods of MJOs,

which acted to limit the development of deep convection. In contrast, during the suppressed periods at the equator, convection developed and built up to 400–300 hPa over *Mirai* (Fig. 10c) owing to moisture convergence along the ITCZ (Fig. 8c). Over Gan and *Reville* (Figs. 10a,b), the troposphere was moistening upward prior to MJO onset with a pace similar to the convective deepening (Figs. 8a,b). Shallow convection in the suppressed phase might help to moisten the lower troposphere and thus provide a more favorable environment for subsequent convection and further moistening (Kiladis

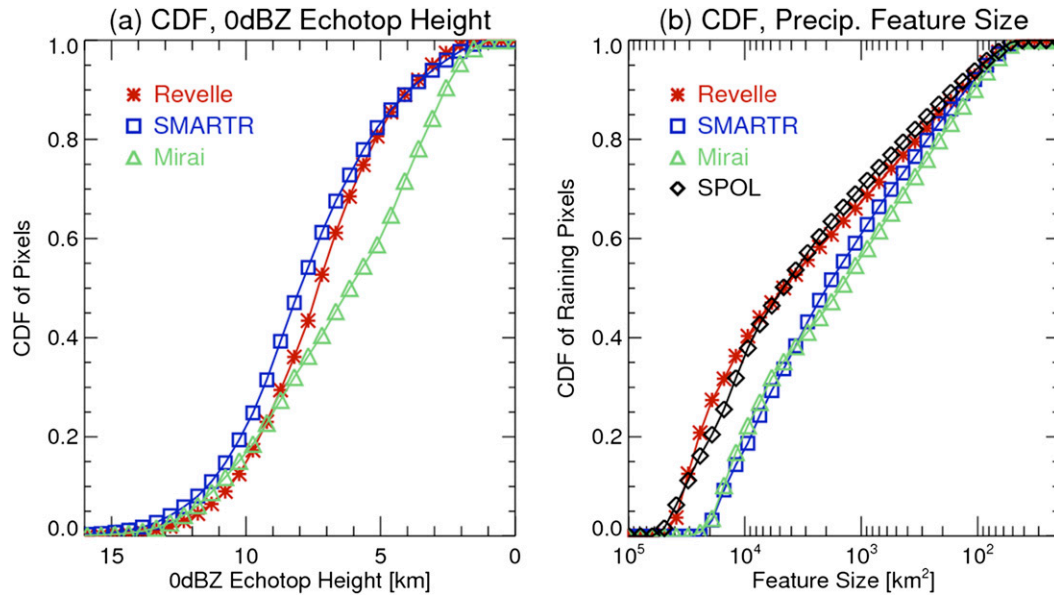


FIG. 9. Cumulative distribution function of radar echoes: (a) pixels as a function of 0-dBZ echo-top height and (b) precipitation occurrence as a function of PF feature size. Note that SMART-R data are restricted to a 180° sector.

et al. 2005; Tian et al. 2006). Eventually, the column becomes sufficiently moist (up to 200 hPa) to support deep convection (up to similar altitude) and widespread MJO convection ensues.

SSTs and low-level winds varied as a function of time significantly over Gan and *Reville* because of the passage of MJOs (Fig. 11). During MJO 1 and 2, SSTs and winds were relatively constant with time (on intra-seasonal scales) over *Mirai* until mid-December indicating subtle influence from the MJO (Fig. 11c). In addition, the mean SST at *Mirai*'s location was about 1°C lower than that at the equator. The sudden increase of SST (in mid-December) at *Mirai* could be due to horizontal advection of warmer water from the north or downwelling oceanic Rossby Wave activity (Webber et al. 2010). The downwelling Rossby wave can increase SST through a reduction of upwelling or entrainment cooling by deepening the thermocline (Xie et al. 2002). Sometimes, the oceanic Rossby wave and lateral advection are also found to cool the SST rapidly (Seiki et al. 2013).

Around Gan and *Reville*, SSTs showed different trends compared to the low-level zonal winds, especially for MJOs 1 and 2 (Figs. 11a,b). The increase of SSTs was mainly during periods of reduced surface winds (e.g., 5–10 October and 15–20 November at Gan and 15–20 November at *Reville*). Maximum SSTs lead maximum precipitation by a few days, indicating the potential role of warm SSTs in preconditioning the region for deep convection and heavy precipitation. As also discussed

earlier, SSTs in the CIO lead the total rainfall by one MJO phase (Figs. 5 and 6) as increases in SST warm and moisten the lower boundary layer through surface evaporation. In contrast, the rapid decrease of SSTs corresponded to development of strong westerly winds in the lower troposphere—that is, westerly wind bursts (e.g., late November). MJOs 1 and MJO 2 are significantly different in terms of SST and wind structures. During MJO 1, SST was relatively steady in the early period of heavy precipitation (18–22 October), evidently because of light wind speeds that accompanied the precipitation events, despite widespread rainfall to the ocean's surface. SST values decreased starting with the onset of stronger near surface winds, especially at *Reville* (24–28 October). During the early heavy precipitation phase of MJO 2 (15–20 November), winds were light and SSTs increased by about 1°C. A sharp decrease in SST occurred with the passages of the two Kelvin wave structures containing peak hourly averaged winds to 15 m s⁻¹ (24–30 November). Moum et al. (2014) carefully documented the role of subsurface mixing (driven by strong near surface winds) in reducing the SST values in MJO 2. After MJO 2, SSTs never recovered to the previous level, thus MJO 3 formed under lower SST conditions. Of course, the cooling (warming) of SSTs can also be contributed by other factors such as increases (decreases) in precipitation and increased (decreased) cloud cover.

Figure 12 depicts the time–height cross section of vertical air motion (omega) over the three sites derived from the CSU-DYNAMO gridded analyses

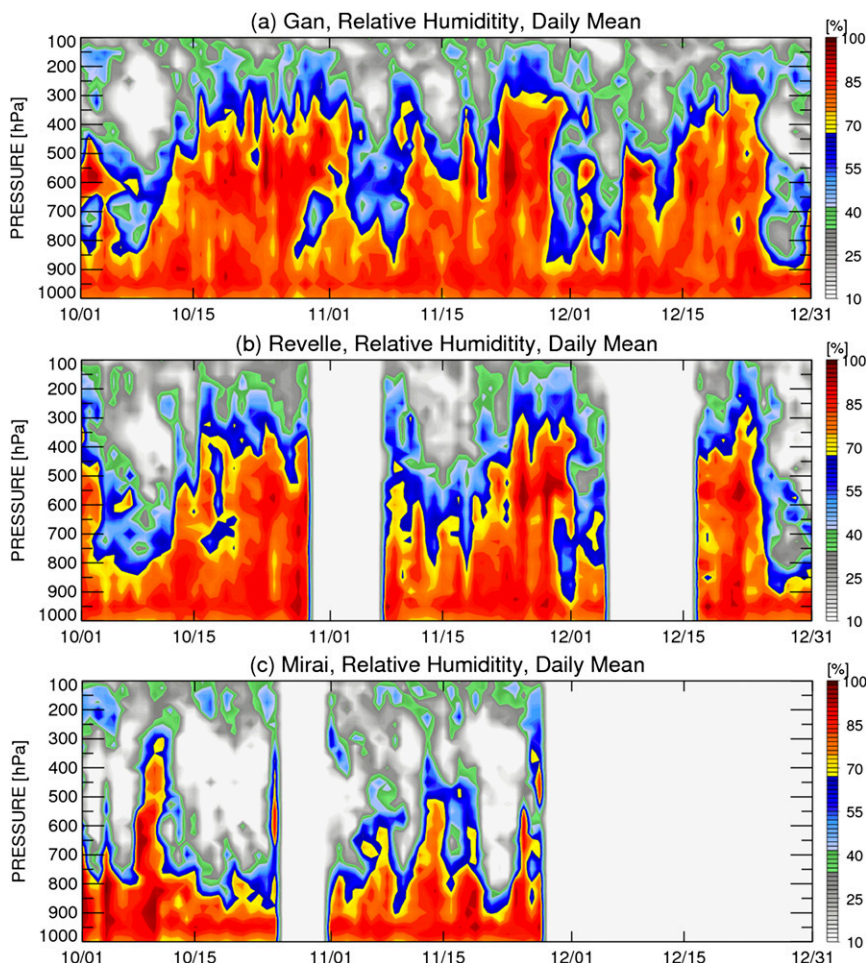


FIG. 10. Time–height cross section of relative humidity (daily mean) from soundings launched at (a) Gan Island, (b) *Revelle*, and (c) *Mirai*. Note that there are data gaps for *Revelle* (30 Oct–8 Nov and 5–16 Dec 2011) and *Mirai* (26–29 Oct and after 29 Nov 2011).

(Ciesielski et al. 2014). Vertical air motion patterns can generally explain the particular evolution of precipitation and echo-top heights. During all MJOs, significant subsidence (upward motion) occurred over Gan and *Revelle* during convectively suppressed (active) MJO periods (Figs. 12a,b). During active periods of MJOs 1 and 2, weak upward motion to subsidence mostly dominated over the *Mirai* location. Subsidence over *Mirai* (off the equator) is speculated to be caused by the deep convection at the equator, which produced sinking motion off the equator. Deep convection around *Mirai* mostly developed during suppressed MJO periods, while shallow and isolated convection dominated during active MJO periods when deep convection persisted at the equator. These features can be more directly seen from the south–north cross sections of vertical air motion derived from the DYNAMO sounding array (Fig. 13). For example, during 5–12 October (active ITCZ convection) the area in the CIO between 10°S and the

equator was characterized by upward motion while regions near and north of the equator were dominated by subsidence (Fig. 13a). In contrast, during active MJO periods (e.g., 18–25 October and 20–26 November) substantial upward motion dominated from 5°S to 10°N, while latitudes south of 7°S were dominated by weak upward motion or downward motion.

d. Composites based on MJO phase

Figure 14 shows the evolution of convective parameters and SST as a function of MJO phase (WH index) over areas 150 km in radius around the three radar sites. Generally, Gan and *Revelle* exhibit a similar evolution pattern with all the convective parameters and SST increasing substantially toward the MJO active phase (phases 1 and 2) and decreasing dramatically afterward (Figs. 14a,b). Maximum SST tends to lead the deepest convection and heaviest precipitation by approximately one MJO phase at least at Gan and *Revelle*. SST

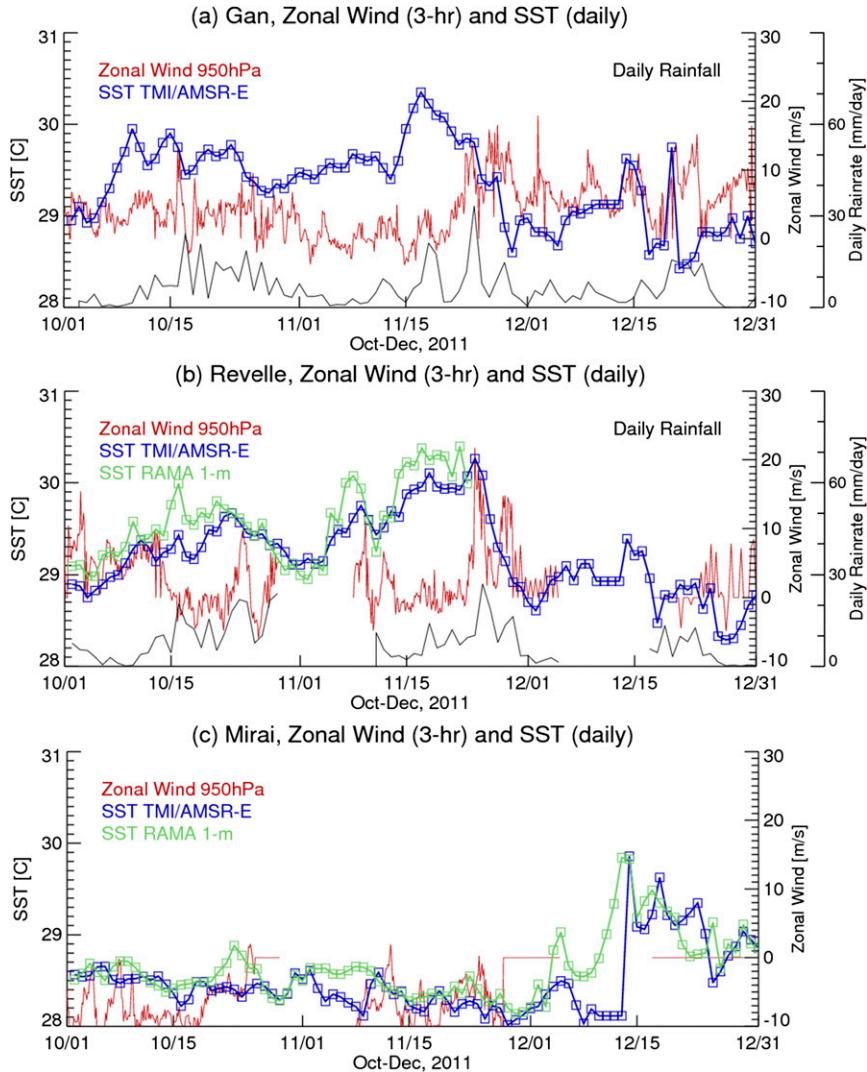


FIG. 11. Time series of low-level winds (at 950 hPa) coupled with SSTs from satellite estimate and/or RAMA buoy: (a) Gan Island, (b) *Revelle*, and (c) *Mirai*. Satellite SST is averaged in a 100 km × 100 km box around the specific site. Note that there are data gaps for *Revelle* (30 Oct–8 Nov and 5–16 Dec 2011) and *Mirai* (26–29 Oct and after 29 Nov 2011).

increases likely played an important role in convective deepening, as SST increases can warm and moisten the boundary layer through surface evaporation. Gan and *Revelle* captured the evolution of MJO convection and environmental conditions (more environmental conditions are shown in Figs. 10–12), as MJO convection passed over Gan and *Revelle* (Figs. 1 and 2). In contrast, convective evolution shows nearly an opposite trend over *Mirai* (Fig. 14c), with convective parameters maximized during suppressed MJO periods and minimized when MJO convection was active near the equator. SSTs at *Mirai* were nearly invariant across different MJO phases, indicating subtle influence from the MJO (also seen from Fig. 11). Otherwise, echo-top heights

(20 dBZ), total rainfall, and lightning still share a similar trend at *Mirai*. Compared to the equatorial sites, the lightning frequency around *Mirai* is significantly lower, although maximum echo-top heights (20 dBZ) are comparable at both locations. This combination of reduced lightning yet similar echo tops suggests that convection near the equator was more intense (Zipser and Lutz 1994).

5. Conclusions

a. Summary and conclusions

This study analyzed radar and sounding data collected from three major research sites during the

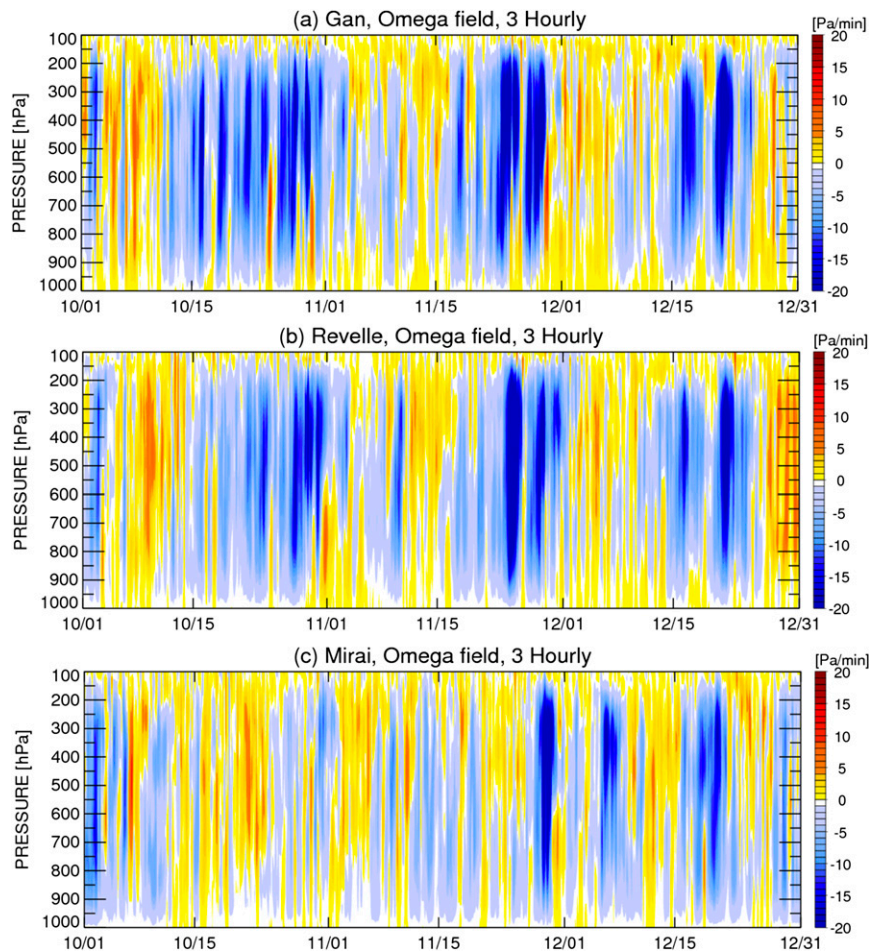


FIG. 12. Time–height cross section of vertical air motion (omega, 3 hourly) derived from the CSU-DYNAMO gridded analyses. Vertical motion is averaged over a $300 \text{ km} \times 300 \text{ km}$ box centered at (a) Gan Island, (b) *Revelle*, and (c) *Mirai*.

2011/12 DYNAMO/CINDY2011 field campaign. These radar–sounding networks were located along the equator and in the vicinity of the ITCZ in the CIO. When combined with large-scale satellite data, observations from the radar–sounding networks resolve the spatial variability of convection associated with the broad MJO convective envelope ($\sim 1000 \text{ km}$). Major variations are found between locations at the equator and south of the equator ($\sim 800 \text{ km}$ away), which can be summarized by Fig. 14. Generally, during MJO suppressed periods, deep convection developed at the *Mirai* location, possibly associated with active ITCZ convection south of the equator. After MJO onset, deep MJO convection at the equator might have induced subsidence over *Mirai* (off the equator), thus suppressing convection over *Mirai* (Fig. 14). There are also slight variations in the phase and magnitude of convective parameters between Gan and *Revelle* during MJO passages. For example, tropospheric moistening (Fig. 10)

and convective deepening (Fig. 7) seemed to be more gradual over *Revelle* compared to at Gan. In short, significant spatial and temporal variations of MJO convection have been found through analyzing the DYNAMO radar–sounding data. Major findings in this study are as follows:

- 1) large-scale satellite data show that heavy rainfall and cold cloud tops associated with warm SSTs were concentrated over areas within 5°S – 10°N from the equator (e.g., Gan and *Revelle*), indicating the passage of core MJO convection over that region; but convection during MJO phases 1 and 2 rarely occurred at locations southward of 5°S (e.g., the *Mirai*'s location at 8°S);
- 2) radar measurements further indicate contrasts between sites at the equator and south of the equator regarding rainfall, echo-top heights, and precipitation morphology, with the equatorial sites having

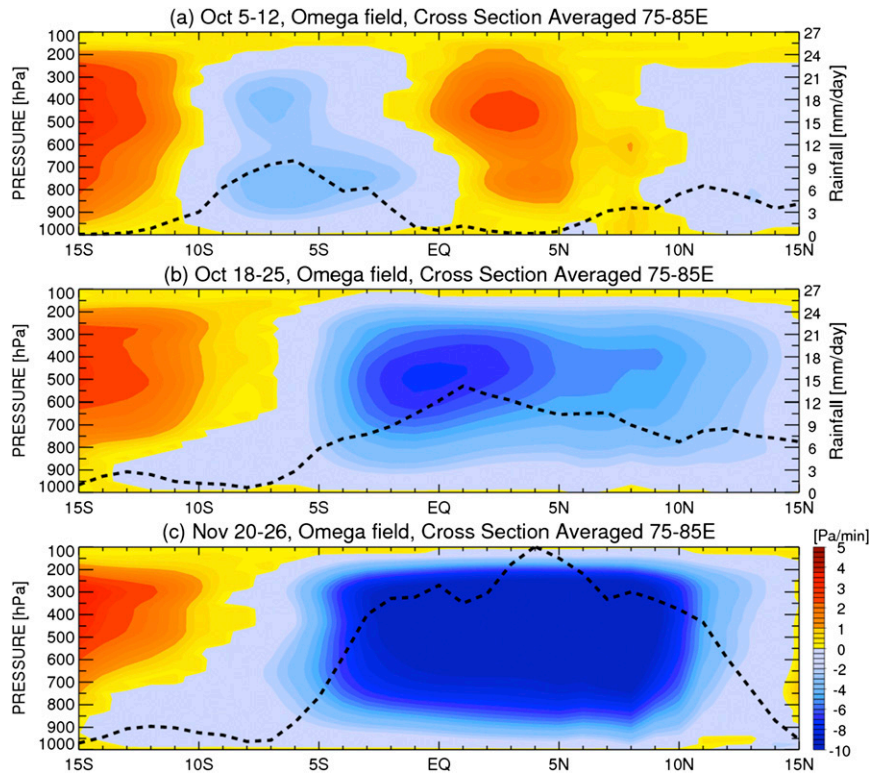


FIG. 13. Latitude–height cross section (mean of 75°–85°E) of vertical air motion (omega) averaged during (a) 15–12 Oct, (b) 18–25 Oct, and (c) 20–26 Nov. Omega is color shaded and TRMM 3B42 daily rainfall is represented by the dashed line. All panels share the same scales and color bars.

strong MJO features while the off-equatorial site exhibits more subtle, remote MJO effects; in addition, there were also substantial differences between equatorial and off-equatorial locations regarding convective properties; for example, *Mirai* observations indicated slightly higher convective rain fractions, considerably more shallow (warm rain) convection, and reduced mesoscale organization;

- 3) *Mirai*'s location also showed little change in environmental conditions due to MJO events: tropospheric moistening occurred during the suppressed MJO periods mostly as a result of ITCZ convection; zonal winds stayed light during active MJO periods and were mostly easterlies; SST remained constant without significant impacts from extensive clouds, heavy precipitation, and surface westerly wind bursts, which were observed near the equator; there was significant subsidence during the active periods of MJO events at the off-equatorial location likely caused by deep convection along the equator;
- 4) Gan and *Revelle* shared similar increasing trends in convective depth, stratiform rain fraction, and precipitation feature size during the building periods of

MJO events and decreasing trends after active MJO periods; all these transitions were well correlated to the changes in mid- to upper-tropospheric moisture, SSTs, zonal wind structures, and vertical air motion; and

- 5) there were differences regarding the phase and magnitude of convective parameters between SMART-R and the *Revelle* radar during the passage of MJO events. Rainfall, echo-top heights, and stratiform rain fractions near Gan peaked about one MJO phase earlier compared to *Revelle*; tropospheric moistening and convective deepening were more gradual and prominent over *Revelle* compared to Gan during MJOs 1 and 2; Gan exhibited more variability in the precipitation and echo-top height time series compared to *Revelle* during MJO 1.

b. Discussion

One of the interesting findings in the MJO convective evolution and spatial variability during DYNAMO is that the off-equatorial site (*Mirai*) was characterized by active convection when the equatorial sites were under

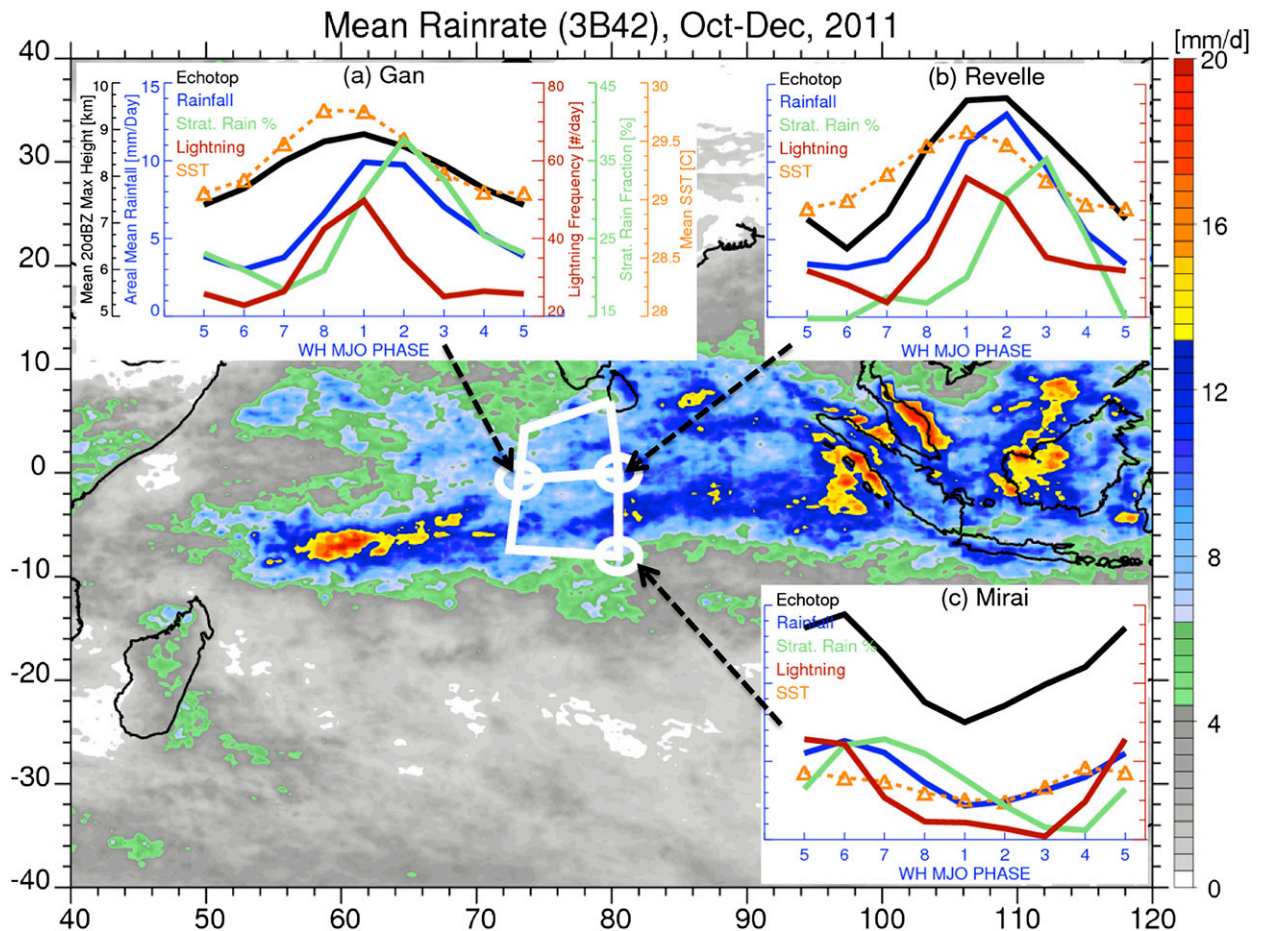


FIG. 14. Map of mean rain rate (mm day^{-1}) over the Indian Ocean from October to December 2011, overlaid by MJO composites of observational parameters over (a) Gan, (b) *Reville*, and (c) *Mirai*: daily maximum 20-dBZ echo-top height (black curves), areal-mean rainfall (blue curves), stratiform rain fraction (green), lightning frequency (red curves), and SST (orange curves). The scales of all parameters are shown in (a).

suppressed conditions, but the off-equatorial site became suppressed after MJO deep convection was established along the equator. Based on results from previous studies and this study, possible processes are proposed here: 1) ITCZ convection located off the equator induced large-scale subsidence over the equator, suppressing the equatorial convection (Yoneyama et al. 2013; Johnson and Ciesielski 2013; Kerns and Chen 2014; also seen in Fig. 13a); 2) convection shifted from the ITCZ to the equator owing to large-scale mechanisms such as a large-scale dry-air intrusion from the subtropics, inhibiting convection in the ITCZ and reducing or eliminating subsidence over the equator (Kerns and Chen 2014); 3) an equatorward shift of convection preconditioned the convective environment and contributed to the initiation of MJO deep convection (Zhang 2005; Kerns and Chen 2014); and 4) deep convection over the equatorial areas associated with active MJO periods produced enhanced

subsidence over ITCZ south of the equator (see Fig. 12, 13b, and 13c).

As mentioned previously, equatorial sites had higher lightning frequencies compared to the *Mirai* location across the MJO life cycle, suggesting convection was stronger in the equatorial areas. This intensity difference may be caused by higher CAPE, the aerosol invigoration effect (Rosenfeld and Lensky 1998; Koren et al. 2008), or both processes working together. First, the equatorial sites had significantly higher CAPE than the off-equatorial site; for example, mean (75 percentile) CAPE values at Gan, *Reville*, and *Mirai* are 1682 (2120), 1877 (2392), and 1074 (1603) J kg^{-1} , respectively. Higher CAPE at the equator could support more intense convection and, thus, a higher lightning frequency. The warmer SSTs at the equator (as shown in Fig. 11) likely contribute to the higher CAPE values through warming and moistening the lower troposphere. However, CAPE at the *Mirai* location was still

significant, suggesting other mechanisms may have served to further increase convective intensity along the equator. The equatorial sites often had higher aerosol concentrations than south of the equator (*Mirai*) because of their closer proximity to India and Sri Lanka, the source region for polluted continental air transported by northerly monsoon flows (DeWitt et al. 2013). As part of ongoing work, aerosol simulations produced by the GEOS-Chem aerosol transport model (Adams and Seinfeld 2002) are consistent with this pattern and further show that CCN concentrations are higher near MJO onset but then quickly decrease via nucleation and precipitation scavenging. Lightning frequency peaks near MJO phases 8 and 1, when CCN concentrations are still appreciable ($\sim 500 \text{ cm}^{-3}$). At the equatorial sites, the higher aerosol (CCN) concentrations could have acted to reduce coalescence growth and promote more robust mixed-phase processes, allowing the release of latent heat via freezing to further invigorate convective updrafts (Williams and Stanfill 2002). However, the cleaner aerosol environment at *Mirai* is consistent with “warm rain” processes (Williams and Stanfill 2002), which act to reduce convective intensity.

This study describes in detail the evolution and properties of MJO convection located at different sites during DYNAMO and provides potential connections to different environmental parameters. This study also raises questions that future research on MJO convection may address. For instance, do SST anomalies have much bearing on the strength of the impending precipitation/convection? How do wind shear, CAPE, and atmospheric moisture determine convective intensity and organization over the equatorial and off-equatorial sites? Statistics derived in this study regarding convective echo height, convective–stratiform precipitation fractions, precipitation system size, rainfall contribution, and their spatial variability can serve to challenge/validate numerical model simulations of MJO convection. When model results agree with observations, the models can be assumed to realistically represent the convection across the MJO life cycle and therefore convective feedbacks to the environment.

Acknowledgments. This research was supported by the National Science Foundation DYNAMO Project Grant AGS-1063928. We thank the entire crew of the R/V *Revelle* and *Mirai* for their excellent support and Chief Scientists James Moum (*Revelle*) and Kunio Yoneyama (*Mirai*) for their dedication and leadership. Special thanks also go to Paul Ciesielski and Richard Johnson for providing the sounding data, sounding-associated products, and science discussion. We also thank Brandon Kerns for help in processing Meteosat satellite data.

REFERENCES

- Adams, P. J., and J. H. Seinfeld, 2002: Predicting global aerosol size distributions in general circulation models. *J. Geophys. Res.*, **107**, 4370, doi:10.1029/2001JD001010.
- Bechtold, P., M. Köhler, T. Jung, F. Doblas-Reyes, M. Leutbecher, M. J. Rodwell, F. Vitart, and G. Balsamo, 2008: Advances in simulating atmospheric variability with the ECMWF model: From synoptic to decadal time-scales. *Quart. J. Roy. Meteor. Soc.*, **134**, 1337–1351, doi:10.1002/qj.289.
- Biggerstaff, M. I., and Coauthors, 2005: The Shared Mobile Atmospheric Research and Teaching Radar: A collaboration to enhance research and teaching. *Bull. Amer. Meteor. Soc.*, **86**, 1263–1274, doi:10.1175/BAMS-86-9-1263.
- Bladé, I., and D. L. Hartmann, 1993: Tropical intraseasonal oscillations in a simple nonlinear model. *J. Atmos. Sci.*, **50**, 2922–2939, doi:10.1175/1520-0469(1993)050<2922:TIOIAS>2.0.CO;2.
- Chen, S. S., R. A. Houze, and B. E. Mapes, 1996: Multiscale variability of deep convection in relation to large-scale circulation in TOGA COARE. *J. Atmos. Sci.*, **53**, 1380–1409, doi:10.1175/1520-0469(1996)053<1380:MVODCI>2.0.CO;2.
- Ciesielski, P. E., and Coauthors, 2014: Quality-controlled upper-air sounding dataset for DYNAMO/CINDY/AMIE: Development and corrections. *J. Atmos. Oceanic Technol.*, **31**, 741–764, doi:10.1175/JTECH-D-13-00165.1.
- Deng, M., and Coauthors, 2014: Stratiform and convective precipitation observed by multiple radars during the DYNAMO/AMIE Experiment. *J. Appl. Meteor. Climatol.*, **53**, 2503–2523, doi:10.1175/JAMC-D-13-0311.1.
- DePasquale, A., C. Schumacher, and A. Rapp, 2014: Radar observations of MJO and Kelvin wave interactions during DYNAMO/CINDY2011/AMIE. *J. Geophys. Res. Atmos.*, **119**, 6347–6367, doi:10.1002/2013JD021031.
- DeWitt, L. H., D. J. Coffman, K. J. Schulz, W. A. Brewer, T. S. Bates, and P. K. Quinn, 2013: Atmospheric aerosol properties over the equatorial Indian Ocean and the impact of the Madden-Julian oscillation. *J. Geophys. Res. Atmos.*, **118**, 5736–5749, doi:10.1002/jgrd.50419.
- Feng, Z., S. A. McFarlane, C. Schumacher, S. Ellis, J. Comstock, and N. Bharadwaj, 2014: Constructing a merged cloud-precipitation radar dataset for tropical convective clouds during the DYNAMO/AMIE Experiment at Addu Atoll. *J. Atmos. Oceanic Technol.*, **31**, 1021–1042, doi:10.1175/JTECH-D-13-00132.1.
- Fliegel, J., 2012: Quality control and census of SMART-R observations from the DYNAMO/CINDY2011 field campaign. M.S. thesis, Dept. of Atmospheric Sciences, Texas A&M University, 84 pp. [Available online at <http://oaktrust.library.tamu.edu/handle/1969.1/148108>.]
- Fujita, M., K. Yoneyama, S. Mori, T. Nasuno, and M. Satoh, 2011: Diurnal convection peaks over the eastern Indian Ocean off Sumatra during different MJO phases. *J. Meteor. Soc. Japan*, **89A**, 317–330, doi:10.2151/jmsj.2011-A22.
- Gentemann, C. L., F. J. Wentz, C. A. Mears, and D. K. Smith, 2004: In situ validation of Tropical Rainfall Measuring Mission microwave sea surface temperatures. *J. Geophys. Res.*, **109**, C04021, doi:10.1029/2003JC002092.
- , T. Meissner, and F. J. Wentz, 2010: Accuracy of satellite sea surface temperatures at 7 and 11 GHz. *IEEE Trans. Geosci. Remote Sens.*, **48**, 1009–1018, doi:10.1109/TGRS.2009.2030322.
- Gottschalck, J., P. E. Roundy, C. J. Schreck III, A. Vintzileos, and C. Zhang, 2013: Large-scale atmospheric and oceanic conditions during the 2011–12 DYNAMO field campaign. *Mon. Wea. Rev.*, **141**, 4173–4196, doi:10.1175/MWR-D-13-00022.1.

- Guy, N., and D. P. Jorgensen, 2014: Kinematic and precipitation characteristics of convective systems observed by airborne Doppler radar during the life cycle of a Madden-Julian oscillation in the Indian Ocean. *Mon. Wea. Rev.*, **142**, 1385–1402, doi:10.1175/MWR-D-13-00252.1.
- Halverson, J. B., B. S. Ferrier, T. M. Rickenbach, J. Simpson, and W.-K. Tao, 1999: An ensemble of convective systems on 11 February 1993 during TOGA COARE: Morphology, rainfall characteristics, and anvil cloud interactions. *Mon. Wea. Rev.*, **127**, 1208–1228, doi:10.1175/1520-0493(1999)127<1208:AEOCSO>2.0.CO;2.
- Hu, Q., and D. A. Randall, 1994: Low-frequency oscillations in radiative-convective systems. *J. Atmos. Sci.*, **51**, 1089–1099, doi:10.1175/1520-0469(1994)051<1089:LFOIRC>2.0.CO;2.
- Huffman, G. J., and Coauthors, 2007: The TRMM Multisatellite Precipitation Analysis (TMPA): Quasi-global, multiyear, combined-sensor precipitation estimates at fine scales. *J. Hydrometeorol.*, **8**, 38–55, doi:10.1175/JHM560.1.
- Johnson, R. H., and P. E. Ciesielski, 2013: Structure and properties of Madden-Julian oscillations deduced from DYNAMO sounding arrays. *J. Atmos. Sci.*, **70**, 3157–3179, doi:10.1175/JAS-D-13-065.1.
- Katsumata, M., T. Ushiyama, K. Yoneyama, and Y. Fujiyoshi, 2008: Combined use of TRMM/PR and disdrometer data to correct reflectivity of ground-based radars. *SOLA*, **4**, 101–104, doi:10.2151/sola.2008-026.
- Kemball-Cook, S. R., and B. C. Weare, 2001: The onset of convection in the Madden-Julian oscillation. *J. Climate*, **14**, 780–793, doi:10.1175/1520-0442(2001)014<0780:TOOCIT>2.0.CO;2.
- Kerns, B. W., and S. S. Chen, 2014: Equatorial dry air intrusion and related synoptic variability in MJO initiation during DYNAMO. *Mon. Wea. Rev.*, **142**, 1326–1343, doi:10.1175/MWR-D-13-00159.1.
- Kiladis, G. N., K. H. Straub, and P. T. Haertel, 2005: Zonal and vertical structure of the Madden-Julian oscillation. *J. Atmos. Sci.*, **62**, 2790–2809, doi:10.1175/JAS3520.1.
- Kim, D., and Coauthors, 2009: Application of MJO simulation diagnostics to climate models. *J. Climate*, **22**, 6413–6436, doi:10.1175/2009JCLI3063.1.
- Koren, I., J. V. Martins, L. A. Remer, and H. Afarog, 2008: Smoke invigoration versus inhibition of clouds over the Amazon. *Science*, **321**, 946–949, doi:10.1126/science.1159185.
- Lau, K.-M., and H.-T. Wu, 2010: Characteristics of precipitation, cloud, and latent heating associated with the Madden-Julian oscillation. *J. Climate*, **23**, 504–518, doi:10.1175/2009JCLI2920.1.
- Lin, J.-L., B. Mapes, M. Zhang, and M. Newman, 2004: Stratiform precipitation, vertical heating profiles, and the Madden-Julian oscillation. *J. Atmos. Sci.*, **61**, 296–309, doi:10.1175/1520-0469(2004)061<0296:SPVHPA>2.0.CO;2.
- Liu, C., E. J. Zipser, D. J. Cecil, S. W. Nesbitt, and S. Sherwood, 2008: A cloud and precipitation feature database from nine years of TRMM observations. *J. Appl. Meteor. Climatol.*, **47**, 2712–2728, doi:10.1175/2008JAMC1890.1.
- Madden, R. A., and P. R. Julian, 1971: Detection of a 40–50 day oscillation in the zonal wind in the tropical Pacific. *J. Atmos. Sci.*, **28**, 702–708, doi:10.1175/1520-0469(1971)028<0702:DOADOI>2.0.CO;2.
- , and —, 1972: Description of global-scale circulation cells in the tropics with a 40–50 day period. *J. Atmos. Sci.*, **29**, 1109–1123, doi:10.1175/1520-0469(1972)029<1109:DOGSCC>2.0.CO;2.
- McPhaden, M. J., and Coauthors, 2009: RAMA: The Research Moored Array for African–Asian–Australian Monsoon Analysis and Prediction. *Bull. Amer. Meteor. Soc.*, **90**, 459–480, doi:10.1175/2008BAMS2608.1.
- Mori, S., and Coauthors, 2004: Diurnal land–sea rainfall peak migration over Sumatera Island, Indonesian Maritime Continent, observed by TRMM satellite and intensive rawinsonde soundings. *Mon. Wea. Rev.*, **132**, 2021–2039, doi:10.1175/1520-0493(2004)132<2021:DLRPMO>2.0.CO;2.
- Moum, J. N., and Coauthors, 2014: Air–sea interactions from the westerly wind burst events during the November 2011 MJO in the Indian Ocean. *Bull. Amer. Meteor. Soc.*, **95**, 1185–1199, doi:10.1175/BAMS-D-12-00225.1.
- Nesbitt, S. W., R. Cifelli, and S. A. Rutledge, 2006: Storm morphology and rainfall characteristics of TRMM precipitation features. *Mon. Wea. Rev.*, **134**, 2702–2721, doi:10.1175/MWR3200.1.
- Oye, D., and M. Case, 1995: REORDER: A program for gridding radar data. Installation and use manual for the UNIX version. NCAR/ATD, 30 pp. [Available online at <https://www.eol.ucar.edu/system/files/unixreorder.pdf>.]
- Powell, S. W., and R. A. Houze Jr., 2013: The cloud population and onset of the Madden-Julian Oscillation over the Indian Ocean during DYNAMO-AMIE. *J. Geophys. Res. Atmos.*, **118**, 11 979–11 995, doi:10.1002/2013JD020421.
- Riley, E. M., B. E. Mapes, and S. N. Tulich, 2011: Clouds associated with the Madden-Julian oscillation: A new perspective from CloudSat. *J. Atmos. Sci.*, **68**, 3032–3051, doi:10.1175/JAS-D-11-030.1.
- Rosenfeld, D., and I. M. Lensky, 1998: Satellite-based insights into precipitation formation processes in continental and maritime convective clouds. *Bull. Amer. Meteor. Soc.*, **79**, 2457–2476, doi:10.1175/1520-0477(1998)079<2457:SBIIPF>2.0.CO;2.
- Rowe, A. K., and R. A. Houze Jr., 2014: Microphysical characteristics of MJO convection over the Indian Ocean during DYNAMO. *J. Geophys. Res. Atmos.*, **119**, 2543–2554, doi:10.1002/2013JD020799.
- Said, R. K., U. S. Inan, and K. L. Cummins, 2010: Long-range lightning geolocation using a VLF radio atmospheric waveform bank. *J. Geophys. Res.*, **115**, D23108, doi:10.1029/2010JD013863.
- , M. B. Cohen, and U. S. Inan, 2013: Highly intense lightning over the oceans: Estimated peak currents from global GLD360 observations. *J. Geophys. Res. Atmos.*, **118**, 6905–6915, doi:10.1002/jgrd.50508.
- Sakurai, N., and Coauthors, 2005: Diurnal cycle of cloud system migration over Sumatra island. *J. Meteor. Soc. Japan*, **83**, 835–850, doi:10.2151/jmsj.83.835.
- Saxen, T. R., and S. A. Rutledge, 2000: Surface rainfall–cold cloud fractional coverage relationship in TOGA COARE: A function of vertical wind shear. *Mon. Wea. Rev.*, **128**, 407–415, doi:10.1175/1520-0493(2000)128<0407:SRCCFC>2.0.CO;2.
- Seiki, A., M. Katsumata, T. Horii, T. Hasegawa, K. J. Richards, K. Yoneyama, and R. Shirooka, 2013: Abrupt cooling associated with the oceanic Rossby wave and lateral advection during CINDY2011. *J. Geophys. Res. Oceans*, **118**, 5523–5535, doi:10.1002/jgrc.20381.
- Steiner, M., R. A. Houze Jr., and S. E. Yuter, 1995: Climatological characterization of three-dimensional storm structure from operational radar and rain gauge data. *J. Appl. Meteor.*, **34**, 1978–2007, doi:10.1175/1520-0450(1995)034<1978:CCOTDS>2.0.CO;2.
- Thompson, J. E., S. A. Rutledge, B. Dolan, and M. Thurai, 2015: Drop size distributions and radar observations of convective and stratiform rain over the equatorial Indian and west Pacific Oceans. *J. Atmos. Sci.*, **72**, 4091–4125, doi:10.1175/JAS-D-14-0206.1.
- Tian, B., D. E. Waliser, E. J. Fetzer, B. H. Lambriksen, Y. L. Yung, and B. Wang, 2006: Vertical moist thermodynamic structure

- and spatial–temporal evolution of the MJO in AIRS observations. *J. Atmos. Sci.*, **63**, 2462–2485, doi:10.1175/JAS3782.1.
- Vialard, J., G. R. Foltz, M. J. McPhaden, J. P. Duvel, and C. de Boyer Monégut, 2008: Strong Indian Ocean sea surface temperature signals associated with the Madden-Julian oscillation in late 2007 and early 2008. *Geophys. Res. Lett.*, **35**, L19608, doi:10.1029/2008GL035238.
- Vitart, F., and F. Molteni, 2010: Simulation of the Madden-Julian oscillation and its teleconnections in the ECMWF forecast system. *Quart. J. Roy. Meteor. Soc.*, **136**, 842–855, doi:10.1002/qj.623.
- Waliser, D. E., and C. Gautier, 1993: A satellite-derived climatology of the ITCZ. *J. Climate*, **6**, 2162–2174, doi:10.1175/1520-0442(1993)006<2162:ASDCOT>2.0.CO;2.
- Webber, B. G. M., A. J. Matthews, and K. J. Heywood, 2010: A dynamical ocean feedback mechanism for the Madden-Julian Oscillation. *Quart. J. Roy. Meteor. Soc.*, **136**, 740–754, doi:10.1002/qj.604.
- Wheeler, M., and H. H. Hendon, 2004: An all-season real-time multivariate MJO index: Development of an index for monitoring and prediction. *Mon. Wea. Rev.*, **132**, 1917–1932, doi:10.1175/1520-0493(2004)132<1917:AARMMI>2.0.CO;2.
- Williams, E. R., and S. Stanfill, 2002: The physical origin of the land–ocean contrast in lightning activity. *C. R. Phys.*, **3**, 1277–1292, doi:10.1016/S1631-0705(02)01407-X.
- Xie, S.-P., H. Annamalai, F. A. Schott, and J. P. McCreary Jr., 2002: Structure and mechanisms of South Indian Ocean climate variability. *J. Climate*, **15**, 864–878, doi:10.1175/1520-0442(2002)015<0864:SAMOSI>2.0.CO;2.
- Xu, W., and S. A. Rutledge, 2014: Convective characteristics of the Madden-Julian oscillation over the central Indian Ocean observed by shipborne radar during DYNAMO. *J. Atmos. Sci.*, **71**, 2859–2877, doi:10.1175/JAS-D-13-0372.1.
- , and —, 2015: Morphology, intensity, and rainfall production of MJO convection: Observations from DYNAMO shipborne radar and TRMM. *J. Atmos. Sci.*, **72**, 623–640, doi:10.1175/JAS-D-14-0130.1.
- Yoneyama, K., C. Zhang, and C. N. Long, 2013: Tracking pulses of the Madden-Julian oscillation. *Bull. Amer. Meteor. Soc.*, **94**, 1871–1891, doi:10.1175/BAMS-D-12-00157.1.
- Zhang, C., 2005: Madden-Julian Oscillation. *Rev. Geophys.*, **43**, RG2003, doi:10.1029/2004RG000158.
- , 2013: Madden-Julian oscillation: Bridging weather and climate. *Bull. Amer. Meteor. Soc.*, **94**, 1849–1870, doi:10.1175/BAMS-D-12-00026.1.
- Zipser, E. J., and K. R. Lutz, 1994: The vertical profile of radar reflectivity of convective cells: A strong indicator of storm intensity and lightning probability? *Mon. Wea. Rev.*, **122**, 1751–1759, doi:10.1175/1520-0493(1994)122<1751:TVPORR>2.0.CO;2.
- Zuluaga, M. D., and R. A. Houze Jr., 2013: Evolution of the population of precipitating convective systems over the equatorial Indian Ocean in active phases of the Madden-Julian oscillation. *J. Atmos. Sci.*, **70**, 2713–2725, doi:10.1175/JAS-D-12-0311.1.